Modelling the Spectral Effects of Water and Soil as Surface Contaminants in a High Resolution Optical Image Simulation

by

Kristin-Elke Strackerjan

B.Sc. Dalhousie University, 1998

A thesis submitted in partial fulfillment of the
requirements for the degree of Master of Science
in the Chester F. Carlson Center for Imaging Science
Rochester Institute of Technology

July 12, 2006

Signature of the Author ——————————————————

Accepted by ——————————————————
        Coordinator, M.S. Degree Program   Date

CHESTER F. CARLSON CENTER FOR IMAGING SCIENCE

ROCHESTER INSTITUTE OF TECHNOLOGY

ROCHESTER, NEW YORK

<u>CERTIFICATE OF APPROVAL</u>

M.S. DEGREE THESIS

The M.S. Degree Thesis of Kristin-Elke Strackerjan
has been examined and approved by the
thesis committee as satisfactory for the
thesis required for the
M.S. degree in Imaging Science

Dr. John Kerekes, thesis Advisor

Dr. Carl Salvaggio

Mr. Scott Brown

Date

THESIS RELEASE PERMISSION

ROCHESTER INSTITUTE OF TECHNOLOGY

CHESTER F. CARLSON CENTER FOR IMAGING SCIENCE

Title of Thesis:

Modelling the Spectral Effects of Water and Soil as Surface Contaminants in a High Resolution Optical Image Simulation

I, Kristin-Elke Strackerjan, hereby grant permission to Wallace Memorial Library of R.I.T. to reproduce my thesis in whole or in part. Any reproduction will not be for commercial use or profit.

Signature _____

Date

Modelling the Spectral Effects of Water and Soil as Surface Contaminants in a High Resolution Optical Image Simulation

by

Kristin-Elke Strackerjan

Submitted to the
Chester F. Carlson Center for Imaging Science
in partial fulfillment of the requirements
for the Master of Science Degree
at the Rochester Institute of Technology

Abstract

The goal of this research is to introduce selected environmental effects into the Digital Imaging and Remote Sensing Image Generation (DIRSIG) Model. DIRSIG is a first principles based synthetic image generation model that produces spectral images in the 0.3 to 14 micron region of the electromagnetic spectrum. It is capable of producing high resolution images using Computer Aided Design (CAD) models of buildings, vehicles, trees, etc. Currently, these objects are modelled in a pristine manner and there is no option to simulate them after exposure to environmental effects.

The current spectral database contains spectral measurements of a wide variety of materials but only under dry and pristine conditions. This has allowed for the modelling of scenes that are radiometrically correct only under those conditions. While this has not been a small task by any means, there is a definite need to simulate images with objects as they can appear in the real world with realistic surface contaminants. Measurements of a variety of materials commonly found in an urban scene were made with varying degrees of contamination. The materials were asphalt, concrete, painted metal and roofing material. The environmental effects that we chose to model were dust

and rain, which translated to sand and water for our measurements. Each combination was measured in the reflective and thermal regions.

The spectral effects of these contaminants were measured in the field and laboratory settings by field spectrometers. The field measurements were qualitative and were used to confirm expected trends found in previous research and published results. As anticipated, the results indicated that as the particle size decreased, there was a corresponding increase in reflectance. The layer thickness also created a change in the reflectance. This change was largely dependent on the contrast between the surface and the contaminant as well as the particle size.

Water was somewhat more challenging for several reasons, one being that there is very little published on the effect of thin layers of water on surface reflectance. Since very little water on a surface causes the layer to act as a blackbody in the thermal region, the amount of water added to the surface had to be done in small increments.

After the qualitative assessment was complete, quantitative measurements in the laboratory were made. New techniques using the field instruments were developed to allow for their use in the laboratory. The results in the laboratory further emphasized the anticipated trends as well as validated the new instrument techniques.

In implementing the models for a varying amounts of soil and water, respectively, on a surface, we developed the mathematical functional relationship between the amount of contaminant on a surface and the spectral reflectance. It was determined that the relationship was highly dependent on the material upon which the sand or water was placed. Knowing what the individual relationships were we then modelled a variety of contamination levels for incorporation into DIRSIG.

As a demonstration of the environmental effects, we chose to model asphalt with each of the contaminants to incorporate into the scene. The validation was done by

comparing a ratio of reflectance spectra for similar surface conditions, contaminated to not, in the simulated and empirical measurements. The simulated measurements were drawn from the DIRSIG scene and the empirical measurements obtained via RIT's airborne sensor, the Modular Imaging Spectrometer Instrument (MISI). The ratios from each set revealed that the DIRSIG image produced results comparable to those in the MISI image. As a result, it is anticipated that the results from this research will allow for the first time the modeling of more realistic scenes of interest to the remote sensing community.

Acknowledgements

There are many wonderful people who have been part of my life here at RIT and now is my chance to mention them. My committee members, Dr Kerekes, Carl and Scott, were wonderful to work with and made it possible to get all of this done in such a short time. Thank you to the measurements team, Lon Smith, Sarah Paul, Mike Fuller and the high school interns, for helping me "wash cars", to Pogo for all his work on the DIRSIG scene generation, and to my wonderfully diverse office mates for an education within and beyond the scope of Imaging Science. Don Taylor, Cindy Schultz, Sue Chan and Sarah Paul - thank you all for a list of things too long to mention here. Last, but not least, thank you to the Department of National Defence and the Canadian Forces for providing this incredible opportunity.

Thank you to two guys who never stop moving but always make time for me, Papa and Lucas. Steve - you have been an incredible source of support and encouragement for which I am very grateful. Thank you also for pretending to understand why I think Maths and Physics are cool! And Monty... thanks for making sure that I got out to play a little everyday.

Contents

List of Figures

List of Tables

Chapter 1

Introduction

The primary interest of this research is to introduce environmental effects into the Digital Imaging and Remote Sensing Image Generation (DIRSIG) Model [`www.dirsig.org`]. DIRSIG is a first principles based synthetic image generation model that produces spectral images in the 0.3 to 14 micron region of the electromagnetic spectrum. It is capable of producing high resolution images using Computer Aided Design (CAD) models of buildings, vehicles, trees, etc. Currently, these objects are modelled in a pristine manner and there is no option to simulate them after exposure to environmental effects.

Ideally, we would like to be able to choose a material, change its surface conditions and obtain the resulting reflected or emitted spectrum. There are several approaches that may be taken to tackle this problem and many different environmental effects that could be considered. In order to limit the scope of this research, we have a chosen a couple of areas to focus on that fall under the larger umbrella of environmental effects.

Let's begin by discussing what the larger umbrella covers. Figure 1.1 provides the taxonomy of environmental effects. There are two main categories: target and
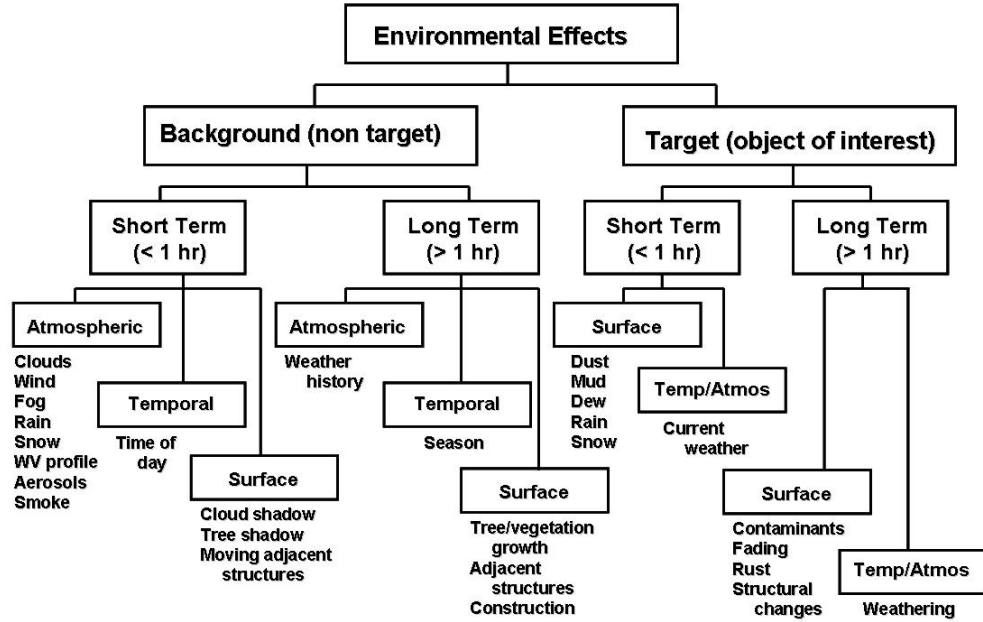
Figure 1.1: Environmental effects taxonomy

background. The target is of primary interest in a scene and in most remote sensing work, but the background must also be well understood. One of the reasons is that the background may have an influence on the target of interest. Directly, surface contaminants will have an effect on the material's surface but there may also be a larger effect on the surrounding scene. Due to the resolution of many airborne platforms, pixels are often mixed, containing more than one material at a time. If the surrounding area's surface conditions change, what will the effect be on the target? The adjacency effect is certainly one area for consideration. The background covariance could also be different and this would likely have an effect on matched filter target detection. The target could be anything of interest in a scene, whether natural or manmade. Clearly, the target and background are complements of each other.

These two areas are further divided into sub-categories that are defined by their

duration. Short-term effects are those which are transient in nature. Most weather falls into this category. These effects would show up as changes in successive observations. Long term effects are those that are slow to change with minimal differences observed in repeated observations over a short timescale. These effects would have to be monitored over a longer period of time to have measurements of significant difference to compare. These categories are also sub-divided into atmospheric, surface and temporal effects. Simply, these are effects that occur in the atmosphere, on the surface of a material and due to time, respectively. As shown in the figure above, weather conditions as well as other atmospheric conditions, such as fog and smoke, are captured by the atmospheric effects category. The surface effects are somewhat more widespread in the types of effects that may be considered. Over short timescales, shadows, adjacent structures and surface contaminants like rain and dust are more important than vegetation growth or fading and rust which occur over longer timescales. Lastly, temporal effects may be on the order of time of day to seasons. Effects such as weathering and the current weather could also be important.

Work to date has focused on obtaining accurate spectral measurements of a wide variety of materials but usually in a pristine condition and has allowed for the modelling of scenes that are radiometrically correct. While this has not been a small task by any means, there is a definite need to expand these results. This is where our environmental effects research comes in. Since pristine surfaces rarely exist in nature, it is necessary to understand how we may model effects that are not within our control. Modelling may be used as a stepping stone to understanding how the effects themselves may alter a scene. The figure above highlights a number of possible effects beyond the scope of this thesis project. As a first step, we have decided to focus on two effects that are present, or may be present, in many scenes. These effects are rain and dust. Water

and sand on surfaces were measured on a variety of substrates to determine the effect of changing amounts of contaminant on the overall reflectance or emissivity.

DIRSIG will incorporate these modelled environmental effects on a variety of surfaces to offer a more realistic view of the outside world: dirty and wet. This will hopefully be the first step to including more environmental effects within DIRSIG such that a user may apply a contaminant to a material in an arbitrary manner.

Chapter 2

Objectives

The objective of this research is to develop models of the selected environmental effects and implement the results into DIRSIG. The approach used for this research was as follows:
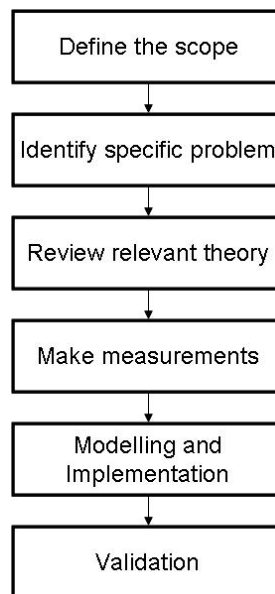
Figure 2.1: Research approach

As previously mentioned, the scope of this task would have been enormous if we attempted to accomplish work on all of the environmental factors in Figure 1.1. For this reason, we narrowed the scope of this work to two effects that are applicable to most surfaces, target or background. We explored the effect that soil and water have on spectral signatures by designing a series of experiments to measure surfaces with soil and water on them. When making remotely sensed measurements, we very rarely have ideal and pristine conditions. It is of interest to model what happens when a surface is dirty or wet, or both. This will allow us to understand how we may compare two images of the same scene when these parameters are changed. It can also have applications in change detection between images.

These two effects present a variety of problems that need to be addressed. Temporal effects will not be addressed at this time. Atmospheric effects cannot be ignored when making measurements outdoors but they will not be specifically isolated for this research either. We are most interested in the surface effects. As an example, the effects of particle size and layer thickness of a soil can be analyzed so that a relationship between each of these and their reflectance spectra may be determined. Limiting our focus to one soil type allowed us to constrain the complexity that may be introduced by different soil composition. Likewise, the amount of water on a surface can affect the signature.

A literature review was done in order to gain an understanding of the theoretical background. The bulk of the material found covered particulate matter since this has been investigated to a greater degree than thin layers of water on surfaces. Research has also been done on the effects of moisture on the reflectance of soils as well as the reflectance characteristics of water alone.

The aim of this research was to make sufficient measurements to use in the modelling

of the effects of these contaminants on material reflectance spectra. We have made field and laboratory measurements of the two environmental effects previously mentioned over the full optical spectral region, 0.3-14 μm. These are the basis upon which we have built the models for incorporation into a DIRSIG scene.

The modelling of these results has allowed us to bring the spectra to life within DIRSIG. The depth to which we have modelled the spectra has depended heavily on the results that we were able to achieve. Using the modelled spectra, we validated the results using field measurements, laboratory results as well as data obtained from one of RIT's airborne sensors, the Modular Imaging Spectrometer Instrument (MISI).

Chapter 3

Background

3.1   Spectral Characteristics of Particulate Soils

We begin by addressing the impact of dust and soil particles on reflectance and emittance spectra. Although a large portion of the previous work has focused on the characteristics of the particles in bulk, not on their interaction as a thin layer with a substrate material, this data can be used to reinforce and validate the findings of our current research. Before we look at what we have accomplished, a review of the previous findings is required. A list of the most pertinent papers that have been written in this area can be found in the bibliography at the end of this thesis project. These form the basis for this section.

Early work on the reflectance properties of soils was summarized by Baumgardner (1985). Several different results are presented in this paper, all of which came to the same general conclusion: as particle size decreases, the reflectance of the surface increases. The greatest increases in reflectance occur for smaller particles, typically those that are 0.4 mm or smaller. Bowers and Hanks (1965) researched the effect of

pure koalinite sample size fractions for $d \sim 0.022$ to 2.68 mm, where d was the particle diameter, on the reflectance and found that the inverse relationship was present. They also found a rapid exponential increase in reflectance at all wavelengths between 0.4 and 1.0 μm with a decrease in particle size. Research done by Hunt and Salisbury (1971) shows that the same effect can be expected for silicate and carbonate materials. They further added that the effect of decreasing the particle size was an increase in reflectance at all wavelengths and also a decrease in the contrast in well-resolved spectral features.

The effect of larger particles on reflectance spectra, particles such as small stones or sand, was researched by Okin and Painter (2004). This work describes the results found by measuring the reflectance spectra of soil particles ranging in size from 50 to 750 μm.
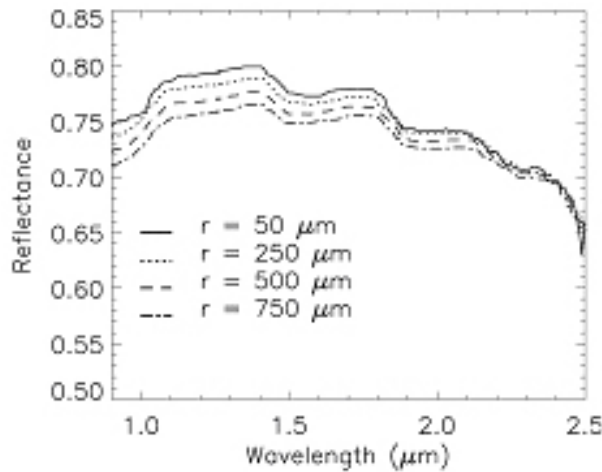
Figure 3.1: Radiative transfer results for quartz grains with rinds of montmorillonite and hematite mixture and grain sizes ranging from 50 to 750 μm [Okin and Painter (2004)]

The results of their work indicate that there is a direct relationship between the particle size and the reflectance. They have made some of the same assumptions as the theory laid out by Hapke (1993) in that the scattering by irregularly shaped particles may be

matched by spherical grains. Mie theory was used to calculate the single scattering properties of the sand grains, such as the scattering phase function, single-scattering albedo and extinction efficiency. Their results indicate that as the grain size decreases, the spectral reflectance increases.

The focus of the Okin and Painter (2004) article was on sand plumes caused by wind erosion from agricultural fields. Using AVIRIS data, they were able to prove the negative relationship between R_{eff} and pixel reflectance. R_{eff}, the effective grain size, was obtained by measuring size distributions of the field samples using standard sieving techniques. Seven stacked soil sieves were used (2.0, 1.7, 1.0, 0.85, 0.5, 0.25, 0.125 mm). Comparing the values received at $\lambda = 1723$ and 2159 nm, the following plot was generated. Although the relationship is not identical at the two wavelengths, it does indicate that the negative relationship exists.
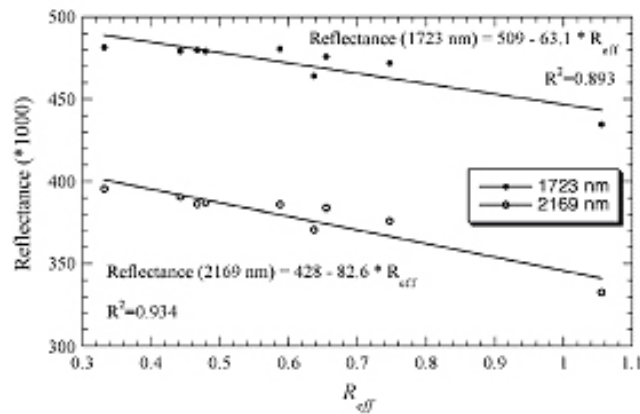
Figure 3.2: Relationships between R_{eff} and scaled AVIRIS reflectance at $\lambda = 1723$ and 2169 nm [Okin and Painter (2004)]

Okin and Painter (2004) also mentioned a relationship between effective particle size and reflectance of sandy soils on the surface. According to their research, the depth at which a layer of sand becomes optically semi-infinite is approximately four times the

effective particle size.

The optical depth of soils is further defined in Satterwhite and Allen (2005). The soils were sieved into various size separates and oven-dried to remove most of the moisture in the samples. Measurements in the reflective portion (0.4-2.5 μm) of the spectrum were made using an ASD Far Range Spectroradiometer (FR2). For consistency, optical depth is defined as the thickness of granular materials measured in millimetres, from which incident light is reflected or transmitted and has a detectable effect on the soil surface reflectance. Below this depth, the incident light is absorbed or infinitely scattered and has no effect on the reflectance signature at the soil surface. Simply, once we can no longer see the effect of the background material on the soil surface reflectance, we have attained the optical depth of that soil.

Using dried Sahara sand separates, the results in the table below indicate that the optical depth is approximately 5-8 times the mean diameter of the particles.

Size Range (mm)	Mean Diameter	Optical Depth (mm)	Particle Layers
1.0-2.0	1.5	7.01	4.7
0.5-1.0	0.75	8.70	11.6
0.25-0.5	0.375	2.00	5.4
0.125-0.25	0.188	1.37	7.3
0.075-0.125	0.10	0.64	6.4
<0.075	0.0375	0.21	5.6

Table 3.1: Optical depths of sand separates for 1.265 μm band
[Satterwhite and Allen (2005)]

This raises an interesting question as to the effect of smaller particles on the reflectance spectra. Smaller particles tend to cling to larger ones and therefore may greatly influence the optical depth of the soil. The findings in the table above indicate that the smaller particles could reduce the optical depth significantly. Particular care must be taken when samples are retrieved for measurement. Soils in nature are naturally sieved by wind and rain, leaving larger particles at the surface. These reflectance

measurements would be very different when taken into the laboratory setting due to the disturbance of the soils during transport. By mixing the soil, the smaller particles coat the larger ones thereby decreasing the optical depth.

Although the focus of Moersch and Christensen (1995) was on the thermal emission from particulate surfaces, they demonstrated that Mie theory, in combination with a Hapke radiative transfer model, provides for the best approximation of measured emissivity spectra. They examined four numerical models of light-scattering processes to laboratory results of particulate samples. The models were: Hapke's reflectance theory converted to emissivity via Kirchhoff's law, Hapke's emission theory, Conel's radiative transfer model, and a hybrid model using Mie single-scattering and Hapke's multiple-scattering emission theory.

One of the findings in this research showed that the mean effective diameter of the particles in a sieved sample was larger than the predicted range of particle sizes. The reason for this is that elongated particles can pass through a screen in a lengthwise direction, thereby increasing the overall particle size distribution. It cannot be assumed that the particles all fall within a certain range simply because the soil was separated using a particular size sieve.

Summarizing the results from Moersch and Christensen (1995), several points can be made. Both the Hapke reflectance and emission models produce similar results. However, since both models were initially derived for grain sizes that are large compared to the wavelength and closely packed, they did not produce the expected results as compared to the measured spectra. The Mie/Conel hybrid model performed somewhat better than the previous two models but it did not correctly model all areas and overestimated the decrease in emissivity with decreasing particle size in the intraband regions. The final model was the Mie/Hapke hybrid. This model performed best over-

all, mainly due to the fact that it combined the single-scattering theory from Mie and the radiative transfer emissivity model from Hapke effectively. The greatest advantage to this model is that it does not require an arbitrary selection of poorly constrained parameters as in the reflection theories. Weak, strong and intraband regions were all modelled very well along with the correct prediction of an emissivity maximum at the Christiansen frequency.

Some full spectrum ($\lambda \sim$ 0.3-25 μm) measurements have been made for hyperfine particles and demonstrate some interesting characteristics in the reflectance spectra. The particles used by Mustard and Hays (1997) were divided into size separates of 5μm increments between 0 and 25μm. The rationale for studying such fine particles is that most planetary surfaces are dominated by particles in this size range and not by larger particles. Mie theory was used to calculate the single-scattering albedo and a Hapke model was used to calculate the reflectance. The particle sizes used in this work demonstrate what happens to the spectra as they transition between different regimes. The effects on scattering and absorption can be examined as processes transition from the geometric optics regime ($d \gg \lambda$) to the regimes where diffraction is more important ($d \sim \lambda$ and $d < \lambda$). Similar to the work done in Moersch and Christensen (1995), Mustard and Hays (1997) used a similar approach to combining Mie and Hapke theories to assess the validity of that approximation for fine reflectance spectra. They were able to model the reflectance spectra fairly well for the both a quartz and olivine sample.

3.2 Moisture Effects on Sandy Soils

Some work has been accomplished by other researchers to demonstrate the effect that moisture has on soil reflectance. Most people who are interested in soils are also interested in being able to identify the constituents of different soils. While this is outside

of our scope, it has lead other researchers to ask just how varying the moisture amount in a soil might affect the shape of the spectral reflectance curves. The following figure shows that an increase in the amount of moisture decreases the spectral reflectance of a soil.
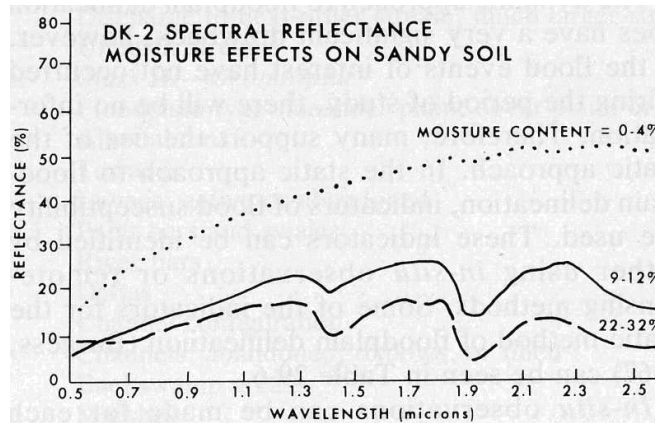
Figure 3.3: Measured spectral reflectances of soils with varying moisture content
[Figure 29-42, Salomonson (1983)]

This decrease is somewhat intuitive for most: add water to a surface and it gets darker. This is the result of a change in the real part of the refractive index, n, from the immersion medium of air $(n = 1.33)$ to water $(n \sim 1.5)$. This decreases the contrast between the soil particles and their surrounding medium and results in an increase in the average degree of forward scattering and therefore an increase in the probability of absorption before re-emerging from the medium. Results in Figure 3.4 further show that increasing the amount of moisture content in a soil results in a decrease in the overall reflectance.
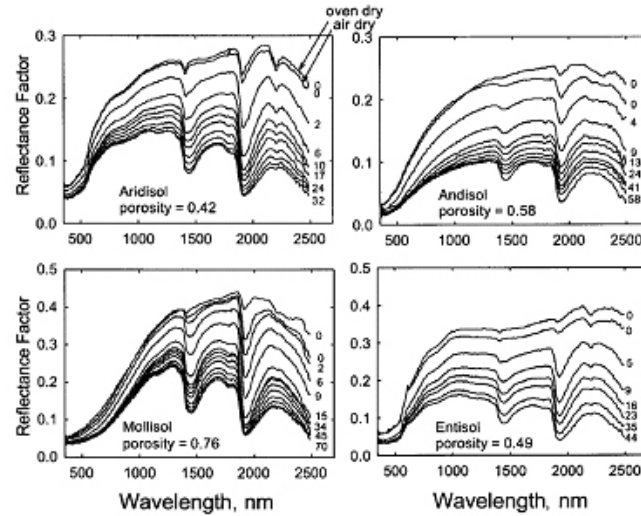
Figure 3.4: Laboratory spectra of four soils with different volumetric water contents (values are percentages by volume) [Figure 1, Lobell and Asner (2002)]

3.3   Thin Layers of Water on Impervious Surfaces

The previous section treated the effect of water on the spectral signature of sandy soils which would allow water to penetrate the surface. This is quite different from the results that one would expect from water on an impervious surface. These surfaces, car hoods, asphalt roads and concrete sidewalks, for example, all allow water to sit on the surface or run-off, as the case may be, but the water may not actually penetrate the surface. We are interested in surfaces such as these and the effect that water might have on their spectral signatures. Therefore we need to take a look at some of the work that has been done in this area. While there is not a lot of published work in this area specifically, Mitchell and Salvaggio (2003) explored the effect that water content can have on the spectral signature in the MWIR and LWIR. Measurements of plastic tarps with and without dew show that there is a significant increase in emissivity when the surface is wet. The question then arose as to how much water would be required to

produce an optically thick layer.

An aluminium sheet with a layer of water on it was weighed and measured as the water evaporated from the surface. The best results are shown in the figure below. These results show that the water increases the radiance of the aluminium sheet almost to the point of becoming a blackbody at the local temperature.
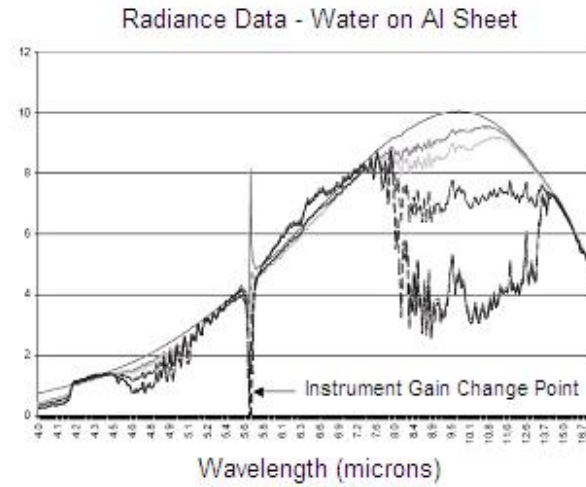
Figure 3.5: Measured radiance $[W/m^2 sr\mu m]$ of thin layers of water on an aluminium sheet: amount of water on the surface increases from the dry aluminium (bottom curve) to the fully saturated surface (top curve) for the spectral range of 4.0 to 17.0 microns [Mitchell and Salvaggio (2003)]

3.4 DIRSIG

The introduction of water and soils on surfaces into DIRSIG will involve a variety of tasks. The following is a brief overview of what DIRSIG does and how results may be implemented. DIRSIG is a first principles based synthetic image generation model that produces multi- or hyper-spectral images in the 0.3 to 14 micron region of the electromagnetic spectrum. The model is designed to produce broad-

band, multi- and hyper-spectral imagery through the integration of a suite of first principles based radiation propagation sub models. These sub models are responsible for tasks ranging from the bi-directional reflectance distribution function (BRDF) predictions of a surface to the dynamic scanning geometry of a line scanning imaging instrument. In addition to sub models that have been specifically created for the DIRSIG model, several of these components (MODTRAN and FASCODE [`www.vs. afrl.af.mil/ProductLines/IR-Clutter`] are the modelling workhorses for the multi- and hyper-spectral community. All modelled components are combined using a spectral representation and integrated radiance images can be simultaneously produced for an arbitrary number of user defined bandpasses.

One of the primary uses of DIRSIG is to produce imagery that may be used to test the accuracy and validity of spectral and spatial image exploitation algorithms. To this end, DIRSIG simulated images may be used to prototype and test algorithms, to test instruments, as an analyst aid, and in many other areas. DIRSIG is capable of introducing texture to a surface by utilizing a large database of varying reflectance curves for a given material. Using a bidirectional reflectance distribution function, the geometry specific reflectance values for all combinations of illumination and observation angles as a function of wavelength may be obtained. Using this information, we are able to define properties of a material that may then be introduced into a scene. Combining the current research with DIRSIG enabled us to model soil and water on surfaces and introduce these environmental effects into a scene.

Chapter 4

Approach

Now that we have a sufficient understanding of the objectives of this research and the background associated with it, the next step is to outline the approach. There has been a significant amount of work done on the analysis of different soils and how to model the effects of particle size and layer thickness. Our work takes a slightly different approach to this analysis because of our end goal: incorporation of our results into DIRSIG. DIRSIG is a one-of-a-kind modelling and simulation tool that allows for various forms of analysis and testing to be performed on synthetic scenes. Because of the accuracy to which DIRSIG is capable of producing real-world, radiometrically correct spectra of various materials, it is an important contributor to the remote sensing community. As such, the measurements that we have taken were used to enhance the ability of DIRSIG to model different materials and surface conditions. Since this is the first step of many in this area, we will not be able to provide a 100% solution for all surfaces and surface conditions. The results provided herein are limited to the environmental effects and the various surfaces that were measured. The approach taken to accomplish these tasks is as follows.

The work may be broken down into three main phases: understanding the theory, making measurements, and modelling. The sections that follow describe how these three phases were tackled and provided the framework for the work that followed.

4.1 Theoretical Understanding

It is very important, when doing research, to understand what others have done before you. To be sure that we were not reinventing the wheel, we reviewed what work has already been published in this area. Previous research has shown that there are definite trends and relationships between the particle size distribution and layer thickness of soils. Repeating some of these measurements with our own instruments and materials gave us our own data set to work with. It also helped to prove to ourselves that we were capable of achieving similar results as other researchers. While published results of measurements are important, it is equally necessary to develop a solid understanding of the theory from a physical or mathematical perspective.

Two findings in particular that were discussed in the background are of immediate use. The first of these is that there is an increase in reflectance with a decrease in particle size. The second point is that a soil is made up of particles which determine its optical depth. There is a point at which the layer of particles is sufficiently thick such that the background no longer influences the reflectance values at any wavelength. Both of these points are mentioned here because they were the basis for the initial measurements, both in the field and in the laboratory. From this point, we were able to determine whether the individual set-ups produced the expected results and how we should proceed with further measurements.

The concepts associated with thin layers of water are somewhat more complex. A basic understanding of what occurs to the reflectance and emissivity values was achieved

through a literature review. The main obstacle was that very little research has been done to examine the properties of thin layers of water and, therefore, there is very little published on the subject. Most researchers in this field are more concerned with large bodies of water such as lakes or oceans. We know that the VNIR and SWIR regions have different properties that influence the reflectance values of water measurements. We also know that the reflectance of soil increases with a decrease in moisture content over the reflective region. In the thermal region, water is a very strong blackbody and the emissivity tends towards 1 when any significant layer thickness is achieved. Reproduction of the anticipated theory is the first step in the measurements section below.

4.2 Making Measurements

Two sections required the bulk of the time and effort for this research: measurements and model implementation. There were two phases to the measurements: field and laboratory. The field measurements required that the skies be clear and consistent, especially for the thermal measurements. The objective was to gain a qualitative understanding of the various set-ups. These results are part of the qualitative results section. The laboratory measurements were performed in a controlled environment and were more quantitative in nature. We will begin by addressing what measurements were made in the field and how they differ from those made in the laboratory.

Soil reflectances may be influenced by three different factors: particle size distribution, layer thickness and areal coverage. Of the these three, only areal coverage has not yet been fully evaluated. Most measurements are made well beyond the soil optical depth and with 100% coverage of the instrument field of view. An assumption that is often made about mixed pixels is that the relationship between the various materials

is linear. The question is whether or not the basis for this lies in actual measurements. We realized that there was a gap in the understanding of the effect of areal coverage on spectral reflectance and the interaction of the soil particles with the material substrate.

Water presents different challenges than soil insofar as measurements in the laboratory. Most instruments that are capable of measuring in the thermal region make use of thermal sources to obtain these spectral measurements. Clearly, if the instrument is in close contact with the sample, evaporation of the water will occur. The particular instrument used to make these measurements and did not require that it be in contact with the sample. The modified set-up used in the laboratory is further discussed below. Like soil, water reflectance may be influenced by a variety of parameters. Layer thickness and areal coverage are the two of primary concern. The water we used in these measurements is considered to be pure and therefore the constituents were not further examined. Water may cover a surface uniformly or, for a smooth surface, as droplets. We chose to examine the effects of changing layer thickness for uniform water coverage.

The Analytical Spectral Devices (ASD) FieldSpec Pro Spectroradiometer and the 102F FTIR Spectrometer from D&P Instruments (D&P) were the two instruments used in both the field and laboratory measurements. The ASD is a field spectrometer that measures the reflectance spectra of surfaces in the VNIR/SWIR region of the spectrum (0.35-2.5 μm). The D&P complements the ASD to cover the full spectrum from 0.35 to 25 μm by providing emissivity measurements from 2 to 25 μm. While both of these instruments are meant for use in the field, techniques were developed to use them in the laboratory. The proper technique used to make these measurements may be found in Chapter 6 of this thesis.

The two surface contaminants, soil and water, were measured on a variety of back-

ground materials. These materials were chosen because they are common to many urban scenes that may be generated in DIRSIG: concrete, asphalt, painted metal and roofing material. The combination of the contaminants and background materials gave us a variety of datasets from which to generate our models.

In the field, the effects of the contaminants were analyzed by making initial measurements of vehicles. Since the vehicles were not cleaned prior to making the measurements, this was considered to be the dirty state. Applying water to the surface created the dirty and wet combination. The surface was dried and cleaned, measured and then water applied to the surface and measured once more. This series of measurements gave the four required surface conditions: dirty and dry, dirty and wet, clean and dry, and clean and wet. Several different vehicles, varying in make and colour, were measured for the qualitative assessment. We also examined the effects of different particle size separates on the overall reflectance of asphalt, as well as the effect of combining soil and water.

Moving into the laboratory, all four materials were measured with soil contamination and only the asphalt and concrete were measured with the water contaminant. The main reason for this was due to a limitation of the measurement set-up that is discussed in Chapter 6.

	Sand	Water
Asphalt	X	X
Concrete	X	X
Painted Metal	X	-
Roofing Shingle	X	-

Table 4.1: Laboratory measurements

The following is a brief description of how the laboratory measurements were made for each of the contaminants. This procedure was followed for both instruments. Since

we were interested in the effect of percentage coverage of soil on the overall reflectance, we measured the reflectance and emissivity of each surface with coverage from 0 to 100%. This was accomplished by placing optically thick piles of the sand, that were approximately one inch in diameter, in the field of view of each of the instruments. A measurement was taken and then the procedure was repeated by adding additional amounts of sand until complete coverage of the field of view was achieved. The figure below illustrates a series of measurements with increasing coverage of the field of view.

Figure 4.1: Increasing soil coverage

Since it was not practical to add water to asphalt and concrete in a percentage coverage manner as we did with the sand, we covered each of the materials completely and simply changed the amount of saturation. We did this by spraying incremental amounts of water on the surfaces and making measurements between each successive application. This simulated an increase in the amount of water that was actually on the surface of the material. As before, we measured the bare, dry surface and continued making measurements until complete saturation was attained.

4.3 Model Development

Once the measurements in the previous section were made, we began modelling the results. There are several approaches that may be used for incorporation into DIRSIG. The approach that we took was to first determine how an increase in sand or water on a surface affected the reflectance. This was done by determining the mathematical

relationship at different wavelengths. We modelled a variety of coverage amounts such that spectra could be pulled from our database of results and applied to an image. In this manner, a region identified as asphalt, for example, would pull spectra from the emissivity file that covers the soil and asphalt mixtures within DIRSIG and apply them to that region.

4.3.1 Implementation

The implementation of these results will be managed by first generating a scene within DIRSIG that contains at least some of the different materials. Using images that already exist, a DIRSIG scene was created. Areas that are known to contain the contaminant and material combinations may be highlighted. The applicable emissivity file is then used to generate the spectra for that region. It is also possible to create areas within the scene that are uniform in coverage.

The required emissivity files are created directly from the measured data. Using digital images of the different coverage amounts for each contaminant-material combination measured in the laboratory, we determined the percentage coverage of each measurement. The functional relationship between percentage coverage and reflectance/emissivity at discrete wavelengths was then calculated and the resulting equations were used to calculate any percentage coverage between 0 and 100%. This method applied regardless of the nature of the relationship, i.e. linear or non-linear, between the coverage amount and reflectance/emissivity.

4.3.2 Modelling

For modelling within DIRSIG, we used the asphalt measurements that were made in the laboratory. Calculating different coverage amounts of the soil on asphalt and water

on asphalt combinations gave us a variety of spectra to work with. The emissivity files were constructed to contain all of the available data from the VNIR/SWIR and LWIR measurements. Several different areas were then isolated within the scene and they each fell into one of two categories: pure or varying contaminant amounts.

The pure contaminant regions were set at given percentage coverage amounts, i.e. 20%, 40%, etc. These areas were used to demonstrate how set percentage coverages could be used within a scene. The second category, varying contaminant amounts, was used to simulate actual occurrences within the scene. A construction site within the region of interest provided for vehicle sand trails leading to and from the site and a large puddle in one of the parking lots allowed us to compare the varying water coverage amounts as well.

4.3.3 Validation

There are a couple of different validations that took place throughout the course of this research. Our preliminary results were validated against previously published results, our measured data was validated against how well we were able to model the data through our own calculations and, finally, the resulting image in DIRSIG was validated against a real data set. The last of these is the validation that we are concerned with in this section. The MISI sensor flies over the RIT campus often and regularly acquires image data. Images that were taken during the course of this research were used to validate the simulated data. Since MISI is not radiometrically calibrated in the VNIR spectral region, we were not able to directly compare the simulated spectral radiances to MISI measurements. However, we were able to compare the derived spectral reflectances and the resulting spectral ratios between the bare and contaminated surfaces.

Chapter 5

Theory

At this point, we will review the theory related to this research. Numerous papers have been written that discuss both field and laboratory results, as well as numerical modelling and empirical results. The theory in each of these areas was examined in order to understand previous work. Using the knowledge obtained from these papers, we prepared an approach specifically for this research. Since we are interested in water and soil coverage of a surface, we must investigate the phenomenology that is intrinsic to these two contaminants. More generally, we need to review characteristics that pertain to particulate media and thin liquid layers.

One significant difference between previous research and this thesis is that we are interested in the effects of varying coverage amounts of the contaminant on the surface of materials of interest, while previous work has focused on the bulk properties of these contaminants. Implications of this difference will be pointed out in the discussion as appropriate.

Particulate matter has been heavily researched and provides us with three distinct factors that may contribute to the overall reflectance: particle size distribution, layer

thickness and areal coverage. The second contaminant, water, is somewhat more diffi-cult to assess. We will, however, review the theory that we do know and how it may be used for surfaces with uniform or non-uniform coverage, i.e. droplets.

The following three categories will be expanded upon in this section: particle size, layer thickness and moisture effects. First we will look at the modelling of dust and soil, and the effect of particle size on reflectance. This area has been investigated thoroughly and has the largest amount of theory associated with it. Since we did not limit the particle size distribution for this work, a simple overview of the effects from different particle sizes on reflectance will be presented in order to gain a basic understanding of the underlying principles. From particle size effects, we will question the effect that layer thickness has on the signature. These two topics cover the primary areas of concern for sand or dust on a surface. Next, we are concerned with moisture effects. How does the introduction of water as a surface contaminant affect the resulting spectra? The amount of water on a surface is certainly important as well as its uniformity of coverage. Although the moisture content in soil has been investigated by other researchers, as seen the Background chapter, we will not delve further into this area.

The theoretical background for this research may be pulled from many sources. The main difference between most of the applicable scattering theories lies in the assump-tions and approximations that are made. All of these theories are attempting to solve the equation of radiative transfer set out by Chandrasekhar in 1960 and any attempt to solve this problem can be quite mathematically rigorous. This equation describes how the intensity of a beam of light changes as it passes through an infinitesimal slab of a medium that can absorb, emit or scatter light. While it is not the purpose of this proposal to review the entire mathematical solution, sufficient mathematical equations will be included in order to provide a useful background.

5.1 Mie vs. Hapke Theory

Both Mie and Hapke scattering theories may be applied to understand and solve the case of particulate media. There are a few distinct differences that are important to point out. One major difference is that Mie scattering describes single-scattering parameters such as the single-scattering albedo, w, and single-scattering phase function $p(g)$. It is mathematically rigorous and requires that the medium consist of well-separated, spherical particles in order to obtain an accurate solution. Hapke theory, on the other hand, describes both single- and multiple-scattering aspects of light scattering. The major assumption behind the Hapke theory is that the particles are large compared to the wavelength of light and they are closely packed. The particles are also not required to be spherical in shape. Diffraction, in this instance, is ignored because the particle cross-sections used in calculating magnitudes of absorption and scattering are the geometrical optics cross-sections. Having said all of this, both of these theories may be used, to varying degrees of success, for purposes that they were not originally intended.

Mie Theory:
Assumes spherical, well-separated particles
Allows for diffraction

Hapke Theory:
Assumes particles are large compared to the wavelength
Allows for irregular particles
Allows for close packing
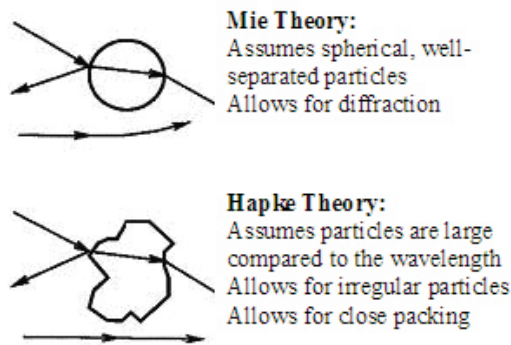
Figure 5.1: Mie vs. Hapke [Moersch and Christensen (1995)]

The basic theory for scattering due to particles is Mie theory. This theory is a highly

forward-scattering description, unlike Rayleigh scattering theory which is symmetric with equal amounts of forward- and back-scatter. Mie scattering occurs when the wavelength of the incident energy (λ) is approximately equal to the size of the particles (D).
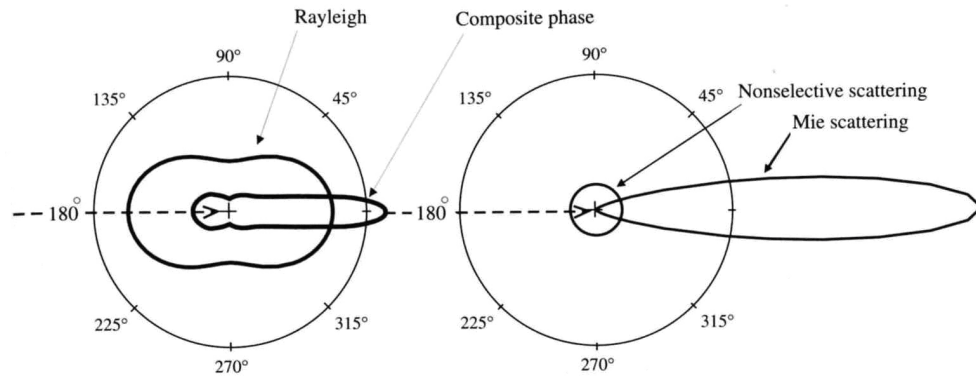
Figure 5.2: Shapes of scattering phase functions [Schott (1997)]

All types of photon-particle interactions are taken into account; however it does not predict the effects that occur when particles are in close proximity to one another. Since Mie theory is a single-scattering theory only, it should only be used to model media where particles are well-separated and at least three radii apart in order to be rigorously correct. Mie single-scattering may also be used to model particulate surfaces where particles are more closely packed, despite this not being its original intent, with some success.

Mie theory is only concerned with two parameters: the size parameter (X) defined below and the refractive index (m) of the particle relative to the surrounding medium, $m = n+ik$. n and k are the real and imaginary parts of the refractive index, respectively. Particles may be defined by their shape, size and general make-up. The mathematical solution to the scattering of electromagnetic radiation by a particle can most easily be

described when it is assumed that the particle is perfect, uniform and spherical. This
ideal case is very rarely found in nature. In order to make this situation more realistic,
we must assume that the majority of the particles in question are irregular in shape,
have rough surfaces and are not uniform in their structure or composition. This is
more realistic, however it presents an enormous computational task to find a solution
to such a problem. When dealing with grains of sand, it is possible to approximate the
size and shape of an irregularly shaped particle as a sphere with an equivalent radius,
a, of:

$$a = \sqrt{\sigma/\pi} \tag{5.1}$$

In (5.1), σ is the geometric cross section of a particle when the average area of the
geometric shadow cast by a particle, randomly oriented in all directions, is measured.
D is the equivalent diameter of the particle and is twice the equivalent radius. This
calculation allows us to approximate the irregular particle as regular in shape. It is
necessary to make such an approximation so that further scattering theories may then
be applied. Particles may be divided into three categories based on their equivalent
diameter. They are either much larger than the wavelength of light, λ, being considered
$(D \gg \lambda)$, about the same as λ $(D \approx \lambda)$, or, finally, they are much smaller than λ
$(D \ll \lambda)$. The ratio of D to λ may be expressed in terms of the size parameter, X:

$$X = \pi D/\lambda \tag{5.2}$$

Depending on the size of the particle of are interest, Mie theory will have different
properties based on how this ratio compares to unity. Three different scattering regimes
are described by Hapke (1993) based on the size parameter. When $X \gg 1$, the diameter
of the particle is much larger than the wavelength of light, and the particle belongs to

the geometric optics scattering regime. For particles that are approximately equal to λ, $X \simeq 1$ and this is the Mie or resonance scattering regime. For clarity, particles with equivalent diameters that are within 10x the wavelength of light are considered to be on the same order. The third regime is the Rayleigh regime and it describes the scattering effects due to particles that are much smaller than the wavelength of light. That is, $X \ll 1$ and $D \ll \lambda$.

Each of these areas is important to the overall signature, but, for the purpose of this study, we are primarily concerned with particles that are larger than or approximately equal to the wavelength of light. Particles that are much smaller than λ are very difficult to manage and are not the focus of this work. In the following section, Mie theory will be expanded upon and related to situations where $D \gg \lambda$ and $D \simeq \lambda$.

The single-scattering albedo of a particle is the ratio of the total amount of power scattered to the total power removed from the wave and is denoted by w. The ratio is then explained using the definitions of the cross sections and efficiencies:

$$w = P_S/P_E = \sigma_S/\sigma_E = Q_S/Q_E \tag{5.3}$$

The subscripts S and E refer to the scattering and extinction components, respectively, of the cross-sections (σ), power (P) and efficiencies (Q). In general, the efficiencies and single-scattering albedo are functions of wavelength. Another convenient quantity is the albedo factor of a medium defined as $\gamma = \sqrt{1 - w}$.

In order to generalize Mie theory, a phenomenological model will be addressed. Numerical evaluations of this theory do exist but are not always practical to use nor do they relate easily to parameters such as the size, shape and complex refractive index of the particle. To begin, the scattering efficiency of a particle is defined as $Q_S = Q_d + Q_s$,

where Q_d is the portion of the scattering efficiency that is associated with diffraction and Q_s is the remainder.

Babinet's principle provides a simple way of interpreting the diffraction of a wave around a particle. For a perfect, isolated sphere, the diffraction efficiency is equal to 1. The diffraction wave around this sphere is equivalent to that through a hole, of the same dimensions as the particle, in an infinite and opaque screen. The total power of the diffraction pattern of the hole is equal to the power passing through the hole. This is true regardless of shape and results in a diffraction efficiency of 1 for the hole. Therefore the diffraction efficiency of each particle in a mixture of isolated, randomly oriented, irregular particles is also equal to 1. For the case where the particles are close together, the diffraction must be associated with the space between the particles and $Q_d = 0$.

The scattering efficiency excluding diffraction, Q_s, for a sphere is defined by Hapke (1993) in equation 5.43 as:

$$Q_s = S_e + (1 - S_e)\frac{1 - S_i}{1 - S_i\Theta}\Theta \qquad (5.4)$$

The S_i and S_e terms, respectively, are the surface reflection coefficients for light that is internally and externally incident light on the particle and Θ is the internal transmission factor. The result of (5.4) is a description of the fractional amount of incident light that escapes from the particle. If the particle were spherical and not irregularly shaped, then S_e would equal S_i.

S_e is the total fraction specularly reflected of the light that is externally incident on the surface of the particle. Once again, a convex particle that has smooth and randomly oriented facets makes the evaluation of S_e much simpler. For real-world surfaces, how-

ever, we must include the effects of surface roughness on the scattering characteristics of the particle. The scale at which these imperfections occur is important. Under most circumstances, if the scale of the roughness is small compared to the wavelength, then the surface may be assumed smooth. One exception that is of particular importance in this work is when k is large, as with metals. In this case, the roughening of the surface will markedly increase the scattering efficiency. The likely cause of this is that the corners and scratches created by the surface roughening act like Rayleigh absorbers. If the scale of the roughness is larger than the wavelength, this introduces an interesting phenomenon. In general, these surfaces still reflect light in a specular direction. That is, the surface characteristics do not change drastically from specular to diffuse. We may, therefore, make a first order approximation of the scattering from the surface of an irregular particle and treat it as specular. S_e is given by the integral of the Fresnel reflection coefficients and may be approximated by:

$$S_e \approx \frac{(n-1)^2 + k^2}{(n+1)^2 + k^2} + 0.05 \tag{5.5}$$

This equation is accurate for $k^2 \ll 1$ and $1.2 \leq n \leq 2.2$.

As previously mentioned, for particles that are very smooth and near-spherical, the internal and external coefficients are the same. The angle at which a refracted ray is incident on the inside of a sphere is equal to that at which it enters the sphere. For an irregularly shaped particle however, the two angles are uncorrelated and S_i is given by the average of the internal Fresnel reflection coefficients over all angles. This integral may be approximated using Snell's Law and some simple mathematical assumptions

about n and k. The result is:

$$S_i \approx 1 - \frac{4}{n(n+1)^2} \qquad (5.6)$$

The approximations for S_i and S_e are compared to their exact solutions in Figure 5.3. As shown, the approximations are good representations of the exact solutions.
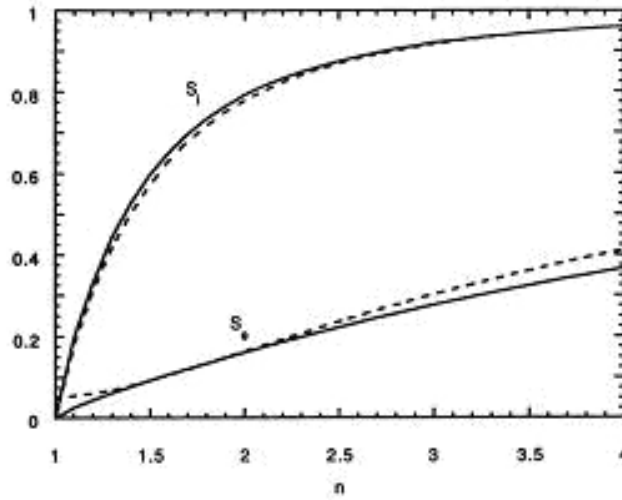
Figure 5.3: External (S_e) and internal (S_i) surface reflection coefficients for $k \ll 1$. The solid lines show the exact solutions and the dashed lines give the approximations. The coefficients and the index of refraction are unitless parameters. [Hapke (1993)]

The internal transmission factor (Θ) is a little bit more complicated. Although particles of interest may not be clear, they are likely to be full of internal scatterers. This means that a ray tracing approach is not necessarily practical or realistic. Instead, Hapke refers us to four different models used to estimate Θ: exponential, Melamed, internal scattering and double exponential. An explanation of each model may be found in Hapke (1993). Based on the experimental design set forth, the exponential and Melamed models do not provide acceptable results for particles larger than $\sim 75\,\mu$m.

The internal scattering and double exponential models both provide excellent fits to the experimental results over the entire range of particle sizes. It would appear that the most versatile and simplest in terms of the number of free parameters is the internal scattering model:

$$\Theta = \frac{r_i + \exp(-\sqrt{\alpha(\alpha + s)})\langle D\rangle}{1 + r_i \exp(-\sqrt{\alpha(\alpha + s)})\langle D\rangle} \tag{5.7}$$

where $r_i = \frac{1 - \sqrt{\alpha/(\alpha+s)}}{1 + \sqrt{\alpha/(\alpha+s)}}$, α and s are the internal scattering and absorption coefficients, respectively, and $\langle D \rangle$ is the length of the average ray that traverses the particle once without being scattered.

5.2   Equation of Radiative Transfer

Now that some of the preliminary terms have been defined, the radiative transfer equation and how it relates to the medium properties may be addressed. The equation is:

$$-\cos\vartheta\frac{\partial I(\tau,\Omega)}{\partial\tau} = I(\tau,\Omega) + \frac{w(\tau)}{4\pi}\int_{4\pi} I(\tau,\Omega')p(\tau,\Omega',\Omega)\,d\Omega'$$

$$+ J\frac{w(\tau)}{4\pi}p(\tau,\Omega_0,\Omega)e^{-\tau/\cos i} + F_T(\tau,\Omega) \tag{5.8}$$

where:

I	is the radiance $[Wm^{-2}sr^{-1}]$,
J	is the irradiance $[Wm^{-2}]$,
p	is the volume phase function,
F_T	is the volume thermal source function $[Wm^{-2}sr^{-1}]$,
τ	is the optical depth,
w	is the volume single-scattering albedo, and
i	is the angle between the incident irradiance and the vertical.

The fundamental assumption of this equation is that the inhomogeneities of the medium emit and scatter radiation independently and incoherently. For a material that

consists of discrete particles that are randomly oriented and positioned this statement is true. (5.8) is the result of summing the contributions of the changes in the powers due to extinction (ΔP_E), scattering (ΔP_S) and emitted radiation (ΔP_F) and equating them to the change in the power that emerges from the top of a cylinder and that which enters at the bottom, $(\partial I/\partial s)ds\, dA\, d\Omega$.

$$\partial I(s,\Omega)/\partial(s) = -E(s,\Omega)I(s,\Omega) + \frac{1}{4\pi}\int_{4\pi} I(s,\Omega')G(s,\Omega',\Omega)\, d\Omega' + F(s,\Omega) \qquad (5.9)$$

Equation (5.9) is the general form of the equation of radiative transfer and the diagrams that follow in Figure 5.4 show how each of these parameters are related to one another. The assumptions needed to get from (5.9) to the complete form of (5.8) will not be discussed here but may be found in Hapke (1993).
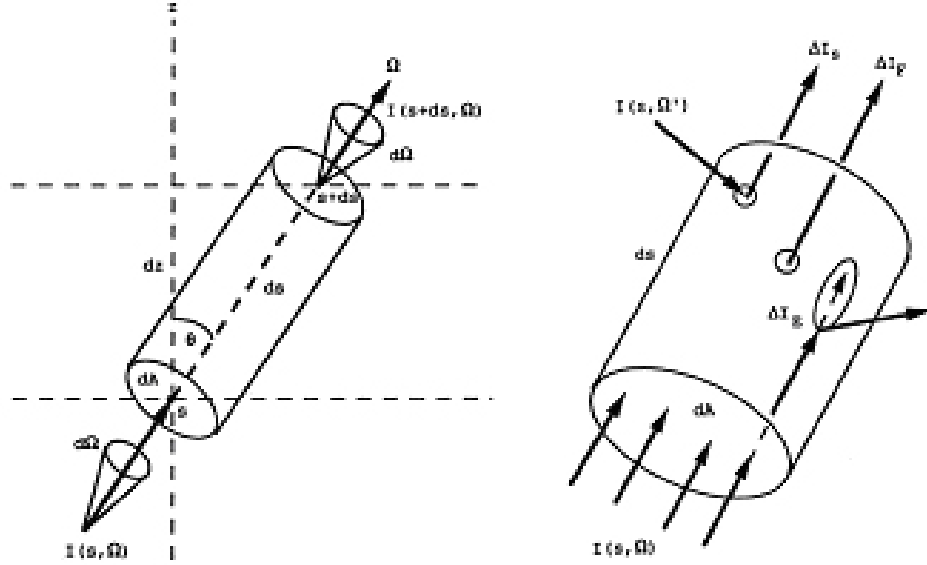
Figure 5.4: Schematic diagram of the radiance [Hapke (1993)]

Now that we have defined the radiative transfer equation, we may address how it

applies to various media and scatterers. Although Hapke (1993) explores many different combinations of particle size and separation, we will focus only on the theory of larger particles (D $\sim \lambda$, D $\gg \lambda$) and for situations where the particles are close together. As mentioned earlier, the region where X $\gg \lambda$ is that of geometric optics. Scattering in this region is greatly affected by diffraction, porosity, shadowing, non-uniform illumination, optical coupling between particles and coherent effects. We will briefly review each of these areas and what role they play in scattering effects.

As the separation between large particles decreases, the diffraction is no longer associated with individual particles. This means that it must be related to the holes in between the particles. When particles are very closely packed, however, the light that is diffracted from one particle cannot be distinguished from the light of the collimated beam that is passing through the holes. This means that we may treat the diffracted light as if it had not been scattered. Q_d may therefore be ignored such that $Q_S = Q_s$, $Q_E = 1$ and there is not a strong forward scattering component that is characteristic of diffraction. Ignoring diffraction holds when $\phi \gg X^{-1}$, where ϕ is the filling factor. The filling factor is defined as the total fraction of the volume occupied by the particles and is equal to $4\pi a^3/3Z^2$, where $Z = N^{-1/3}$ is the mean distance between particles and N is the number of particles per unit volume. $1 - \phi$ is referred to as the porosity.

Non-uniform illumination of large, closely packed particles results in absorption and scattering of the same average fraction of incident light with the same average angular pattern that would have occurred if this same ensemble had been uniformly illuminated. The scattering efficiency and phase angle do not change from the values that were established for isolated particles. An exception exists where one particle shadows another at small phase angles. This introduces a phenomenon referred to as opposition effect.

Optical coupling occurs when particles are so close to one another (within roughly one wavelength of each other) that their internal and external surface reflections are reduced in that region. The fraction of total particle surface that falls within this region is typically so small that it may be ignored. In situations where minerals are brought into intimate contact with one another, such as in a rock, or when they are under extremely high pressure, which may cause non-random orientation of the particles, the optical coupling may not be negligible. Since this is very rarely the case in a laboratory setting, we need not consider it for this research.

Finally, coherent effects are of concern when the wavelength is more closely matched to the particle size. The magnetic and electric fields far away from a spherical particle tend to fall off as $1/r$. Closer to the sphere itself, these fields tend to fall off as $(\lambda/r)^2$. This region is referred to as near-field. Since we are outside of this region insofar as particle size is concerned, we will not delve further into the details of coherent effects.

5.3 Bidirectional Reflectance of a Particulate Medium

We will now turn our attention to the effects of an infinitely thick layer of particulate medium on the bidirectional reflectance. Bidirectional reflectance of a medium is defined as the ratio of the scattered radiance at the detector to the incident irradiance. (5.8) shows that this could be obtained, after some manipulation, from the given parameters. The equation of radiative transfer requires that some approximation and a few assumptions be made in order to achieve anything close to a solution. We will begin by addressing how the scattering from a particle within a semi-infinite medium may be expressed and then move onto the description of a particulate medium of infinite optical thickness. These scenarios will allow us to express general analytical solutions to the equation of radiative transfer.

The following figure depicts how the various terms relate to one another.
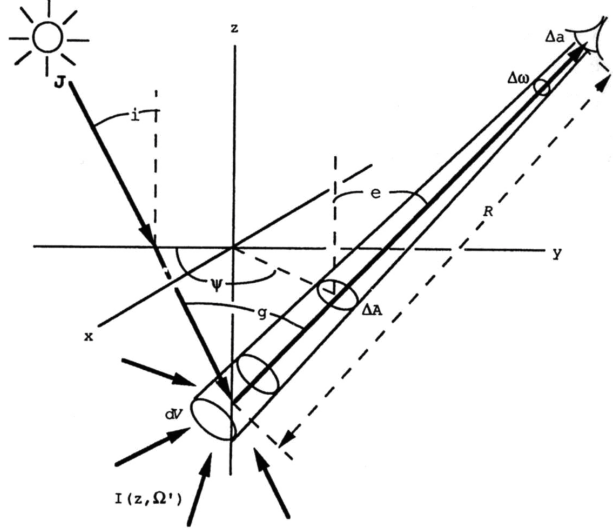
Figure 5.5: Scattering geometry within a particulate medium [Figure 8.4, Hapke (1993)]

The volume element that is described by $dV = R^2 \Delta w dR$ is located at an altitude of z, within Δw and at a distance R from the detector. The volume element is surrounded by radiance, $I(z, \Omega')d\Omega'$, travelling within $d\Omega'$ in the direction of Ω'. The amount of power that is scattered by the particles in dV into the unit solid angle about the direction Ω between dV and the detector may then be defined as:

$$\frac{dV}{4\pi} \int_{4\pi} G(z, \Omega', \Omega)I(z, \Omega')d\Omega' \; , \tag{5.10}$$

where $G(z, \Omega', \Omega)$ is the volume angular scattering coefficient.

As well, an amount of power $F(z, d\Omega)dV$ is emitted from dV per unit solid angle towards the detector. The solid angle of the detector as seen from dV is $\Delta a/R^2$ and the radiance is attenuated by extinction over the distance from dV towards the detector

by a factor of $e^{-\tau/\mu}$. The resulting power from dV reaching the detector is then:

$$dP_D = [\frac{1}{4\pi}\int_{4\pi} G(z,\Omega',\Omega)I(z,\Omega')d\Omega' + F(z,\Omega)]dV\frac{\Delta a}{R^2}e^{-\tau/\mu} \qquad (5.11)$$

The radiance, I_D, at the detector is the power per unit area per unit solid angle and the total power reaching the sensor is the integral of dP_D over all volume elements within Δw between $z = -\infty$ and $+\infty$. This results in the following equation:

$$I_D = \frac{1}{\Delta w \Delta a}\int_{z=-\infty}^{+\infty} dP_D$$

$$= \int_0^{+\infty} [\frac{w(\tau)}{4\pi}\int_{4\pi} p(\tau,\Omega',\Omega)I(\tau,\Omega')d\Omega' + F(\tau,\Omega)]e^{-\tau/\mu}\frac{d\tau}{\mu} \qquad (5.12)$$

The equation of radiative transfer allows us to simplify this even further by assessing the term inside the brackets. Comparing this term with (5.9), we can see that it is equal to:

$$I_D = -[\mu\frac{\partial I(\tau,\Omega)}{\partial \tau} - I(\tau,\Omega)] = -\mu e^{\tau/\mu}\frac{\partial}{\partial \tau}[I(\tau,\Omega)e^{-\tau/\mu}] \qquad (5.13)$$

Since the radiance is finite as $\tau \to \infty$, $I_D = I(0,\Omega)$. This means that the radiance at the detector is the same as the radiance leaving the medium at the $\tau = 0$ level in the direction of the detector.

From here we are can derive the equations using the bidirectional reflectance of a particulate medium of semi-infinite thickness. By neglecting multiple scattering and assuming no thermal sources, the first term in (5.12) and the thermal term from $F(\tau,\Omega)$ may be ignored. This simplifies the equation a fair bit. The total radiance reaching the detector due to single scattering (I_{Ds}) is then:

$$I_{Ds} = J\frac{1}{4\pi}\frac{1}{\mu}\int_0^{\infty} w(\tau)p(\tau,g)e^{-(1/\mu_0+1/\mu)\tau}d\tau \qquad (5.14)$$

If w and p are independent of τ and z, then (5.14) evaluates to:

$$I_{Ds} = J \frac{w}{4\pi} \frac{\mu_0}{\mu_0 + \mu} p(g) \qquad (5.15)$$

If $p(g) = 1$, then the scatterers are isotropic and the equation is called the Lommel-Seeliger law. Equation (5.15) is the general solution which allows for the inclusion of non-isotropic scatterers.

It is important to include multiple scattering for an accurate estimate of the bidirectional reflectance. Hapke describes the changes that occur to the scattered light by defining five different steps Figure 5.6.

This results in an exact, general solution for r with very few assumptions about the medium. The assumptions are that the medium is composed of particles that scatter light isotropically and independently of each other. Combining the results of the exact single-scattering and multiple-scattering contributions to the radiance at the detector for an arbitrary particle phase function results in:

$$r(i, e, g) = \frac{I_{Ds} + I_{Dm}}{J} = \frac{w}{4\pi} \frac{\mu_0}{\mu_0 + \mu} [p(g) + H(\mu_0)H(\mu) - 1] \qquad (5.16)$$

where $H(x)$ is a function that must satisfy $H(x) = 1 + \frac{w}{2} x H(x) \int_0^1 \frac{H(x')}{x + x'} dx'$. I_{Ds} and I_{Dm} are the total radiance reaching the detector due to single and multiple scattering, respectively.

The opposition effect is another part of bidirectional reflectance which needs to be considered. The phenomenon occurs when particles near the surface of a medium cast shadows on those that are deeper. The opposition effect is a sharp surge in brightness which occurs around zero phase angle. As the angle decreases, the shadows that were once visible at larger phase angles are hidden by the objects casting them. In this sense,
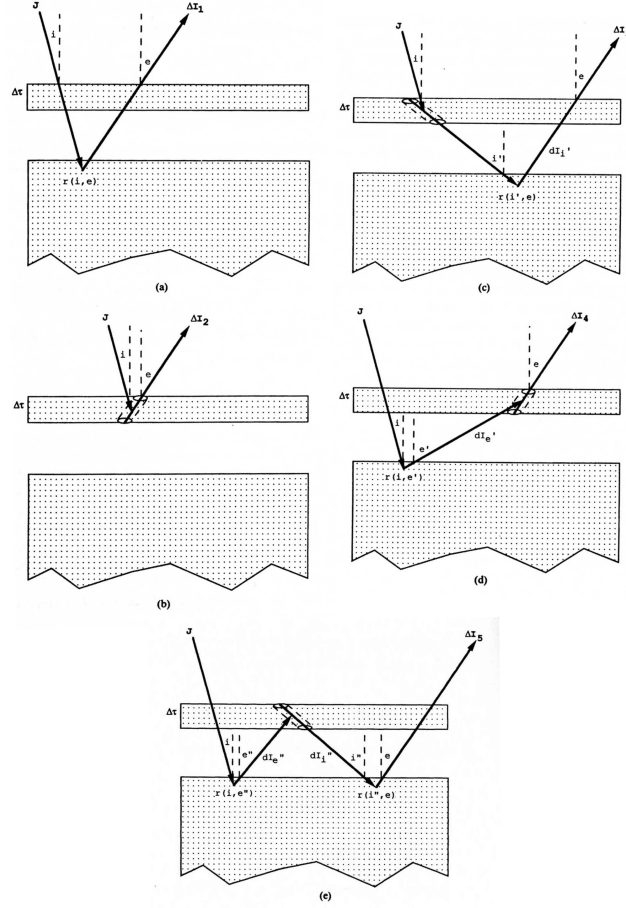
Figure 5.6: Thin layer scattered radiance approximation [Fig. 8.7, Hapke (1993)]

the opposition effect is caused by shadow hiding. The details of the derivation are in Hapke and are summarized by including a term in (5.16) to account for the opposition effect.

$$r(i, e, g) = \frac{I_{Ds} + I_{Dm}}{J} = \frac{w}{4\pi} \frac{\mu_0}{\mu_0 + \mu} \{[1 + B(g)]p(g) + H(\mu_0)H(\mu) - 1\} \qquad (5.17)$$

5.4   Layered Media

One of the materials that we are interested in examining is painted metal, such as that found on vehicles. By simple examination, one can see that the surface of a car reflects light in a variety of different ways. Surfaces such as these are sufficiently smooth when compared to the wavelength of light that light incident on the surface is scattered in a specular manner from the surface and diffusely from the layer below the surface. The specular component in this situation is referred to as regular reflection. In remote sensing, the surfaces in which we are interested may be covered in dust, frost or mist, for example. This requires the analysis of scattering by layered media.

Consider a surface that has two layers: the bottom layer, denoted by a subscript L, is infinitely thick and the upper layer, denoted by a subscript U, has some finite thickness. The boundary conditions require that the radiance must be continuous across the top and bottom surfaces. The general equations that define these radiance are given by:

$$I_1(\tau) = \frac{1}{2}[A(1-\gamma)e^{-2\gamma\tau} + B(1+\gamma)e^{2\gamma\tau}]$$
$$I_2(\tau) = \frac{1}{2}[A(1+\gamma)e^{-2\gamma\tau} + B(1-\gamma)e^{2\gamma\tau}] \tag{5.18}$$

These equations are derived in Hapke (1993) using the two stream approach to scattering. The constants A and B are determined by the boundary conditions, τ is the optical depth, and I_1 and I_2 are the upward- and downward-going radiances in the layer. For the two-layer case, the boundary condition stated above requires that $I_2(0) = I_0$. At the interface of the two layers, $\tau = \tau_0$ and the upwelling radiance must equal the fraction of the downwelling radiance reflected back up from the lower layer, $I_1(\tau_0) = r_L I_2(\tau_0)$. Solving for the constants and using $r_0 = \pi I_1(0)/\pi I_0$, we obtain an

expression for the diffusive reflectance, r_0:

$$r_0 = r_U[(1 + \frac{1}{r_U}\frac{r_L - r_U}{1 - r_L r_U}e^{-4\gamma\tau_0})/(1 + r_U\frac{r_L - r_U}{1 - r_L r_U}e^{-4\gamma\tau_0})] \qquad (5.19)$$

This expression tells us that as the optical depth approaches infinity, the diffusive reflectance approaches that of the upper layer. The converse is also true: as the optical depth becomes smaller and smaller, the reflectance approaches the diffusive reflectance value of the lower layer. The more exposed the lower layer is, the greater an influence it will have on the overall reflectance values, and the more that it is covered by the upper layer, the greater the influence of that upper layer on the reflectance. For our measurements, it was important to understand how much soil was needed to achieve this optical depth.

If the albedo of the lower layer is very low, its reflectance value, r_L , may be set to zero. This further simplifies equations (5.20).

$$r_0 = r_U\frac{1 - e^{-4\gamma\tau_0}}{1 - r_U^2 e^{-4\gamma\tau_0}} \qquad (5.20)$$

At this point, we will briefly mention the significance of mixtures on reflectance values. Since soil can have several different constituents, we need to understand how the reflectance may be affected. In an intimate mixture, the material consists of different types of particles, mixed homogeneously and in close proximity. The reflectance of an intimate mixture is a nonlinear function of the reflectances of the pure endmembers. The parameters in the equation of radiative transfer are the averages of the various types of particles in the mixture weighted by cross-sectional area. As previously mentioned, surface asperities and subsurface fractures may be treated as small particles. As such, using the formulae for intimate mixtures we may determine the effects of these features

on the reflectance. The equations that govern the effects of intimate mixtures may be found in Hapke (1993).

5.5   Thermal Emissivity

The theory in the preceding sections has focused primarily on reflectance measurements. Since we are also interested in what occurs at longer wavelengths, we need to discuss the effects of thermal emission. The region of the spectrum around 10 μm is called the thermal infrared region and many materials exhibit certain characteristics that may only be observed in this region. It is important to note that most of the previous discussion of reflectance theory will also apply to emissivity at the same wavelength due to the complementary nature of the two quantities. Thermal emission need not be considered at shorter wavelengths, $\lambda < 3\mu$m, and reflected sunlight is not an issue at longer wavelengths. In the mid-infrared however, the radiance received by a detector includes both reflected and emitted components.

To begin this discussion, we must review some blackbody radiation theory. Spectral radiance in a hollow cavity, surrounded by a material that is optically thick at all wavelengths and heated to a uniform temperature T, is given by:

$$I(\lambda, T) = \frac{1}{\pi} U(\lambda, T) \tag{5.21}$$

$U(\lambda, T)$ is the Planck function given by:

$$U(\lambda, T) = \frac{2\pi h_0 c_0^2}{\lambda^5} \frac{1}{e^{\frac{h_0 c_0}{\lambda k_0 T}} - 1} \qquad [W/m^3] \tag{5.22}$$

where:

h_0	is Planck's constant and is equal to $6.62{\times}10^{-34}$ Jsec,
c_0	is the speed of light, $2.998{\times}10^8$ m/s,
k_0	is Boltzmann's constant and is equal to $1.381{\times}10^{-16}$ J/K,
$c_1 = 2\pi h_0 c_0^2$	is called the first radiation constant and is equal to $3.742{\times}10^{-16}$ Wm^2, and
$c_2 = h_0 c_0/k_0$	is called the second radiation constant and is equal to 0.01439 mK.

From (5.21), $U(\lambda, T)$ is defined as the power per unit area per unit wavelength interval. The radiance in the cavity is found to be independent of direction, position, shape of the cavity and composition of its walls. The total power per unit area $V(T)$ emitted from the surface of a blackbody can be found by integrating $U(\lambda, T)$ over all wavelengths. Therefore, $V(T)$ equals:

$$V(T) = \int_0^\infty U(\lambda, T)\, d\lambda \tag{5.23}$$

Upon substitution of $x = h_0 c_0/\lambda k_0 T$ into (5.23) and simplifying the integral, we obtain $V(T) = \sigma_0 T^4$. This is known as the Stefan-Boltzmann law and the Stefan-Boltzmann's constant (σ_0) equals $5.671\text{x}10^{-8} W/m^2 K^4$. The ratio of the actual power that is emitted by an optically thick material, $U_a(\lambda, T)$, to that emitted by a perfect blackbody, $U(\lambda, T)$, is called the spectral emissivity, $\epsilon(\lambda)$. If the spectral emissivity of a material is independent of wavelength, then the surface is called a grey body.

The complementary nature of emissivity and reflectance allows us to use one to calculate the other. Specifically, when it is easier and more convenient to measure reflectance than emissivity, we can use reflectance to obtain the emissivity. This relationship is defined by Kirchhoff's law. Using the directional emissivity for this law, the emissivity of a smooth surface is:

$$\epsilon_d = 1 - R(e) \tag{5.24}$$

where $R(e)$ is the average of the Fresnel reflection over the two directions of polarization.

The assumption that transmittance is zero was made and is appropriate for opaque or optically thick materials.

The equation of radiative transfer that was previously derived included a thermal component, F_T. Returning to that equation, we have:

$$-\cos\frac{\partial I(\tau,\Omega)}{\partial\tau} = I(\tau,\Omega) + \frac{w(\tau)}{4\pi}\int_{4\pi} I(\tau,\Omega')p(\tau,\Omega',\Omega)\,d\Omega'$$

$$+J\frac{w(\tau)}{4\pi}p(\tau,\Omega_0,\Omega)\exp(-\tau/\cos i) + F_T(\tau,\Omega)$$

F_T is the volume thermal source function and is defined by $F_T = F_{Te}/E$. The thermal volume emission function, F_{Te}, is the power emitted per unit wavelength per unit solid angle from the volume per volume element and E is the volume extinction coefficient.

After some manipulation, the thermal source function of a particulate medium may be written as:

$$F_T = \frac{\gamma^2(\lambda)}{\pi}U(\lambda,T) \tag{5.25}$$

We will now follow the same approach to derive an equation for the directional emissivity of a particulate medium as we did for the directional reflectance. The derivations required to complete the picture can be found in Hapke (1993) and will not be discussed here. To begin, the directional emissivity, $\epsilon_d(e,\lambda)$, is the ratio of the thermal radiance leaving the surface at a uniform temperature into a given direction e to the thermal radiance emerging from a blackbody at the same temperature. Thus, $\epsilon_d(e,\lambda) = \pi(I(e,\lambda,T)/U(\lambda,T))$. As before, a thin layer of particles is added on top of an infinitely thick layer of the same type of particles.

Upon completion of the derivation, we find that $\epsilon_d(e) = \gamma H(\mu)$. Once again we

arrive at an exact solution that makes no assumptions about the medium other than it is composed of particles that emit and scatter isotropically. Using the previous approximation for $H(\mu)$ and the definition of $\epsilon_d(e, \lambda)$ mentioned above, the radiance that emerges from the surface of an optically thick layer of particles at uniform temperature is:

$$I(e) = \frac{\gamma(\lambda)}{\pi} H(\lambda, \mu) U(\lambda, T) \tag{5.26}$$

Combining (5.25) with (5.8), we have a version of the equation of radiative transfer that now includes the expanded thermal source function term.

$$-\cos \frac{\partial I(\tau, \Omega)}{\partial \tau} = I(\tau, \Omega) + \frac{w(\tau)}{4\pi} \int_{4\pi} I(\tau, \Omega') p(\tau, \Omega', \Omega) \, d\Omega'$$

$$+ J \frac{w(\tau)}{4\pi} p(\tau, \Omega_0, \Omega) \exp(-\tau / \cos i) + \frac{\gamma^2}{\pi} U(T, \tau) \tag{5.27}$$

5.6 Volume scattering, Restrahlen Bands and Christiansen Features

Volume scattering refers to the optical processes that occur when $k \ll 1$ and $n > 1$. These indices of refraction vary for different types of materials based on their chemical composition. They may be used to calculate the anticipated wavelength location of features such as the location of restrahlen bands and Christiansen features. Figure 5.7 shows the values for n and k for a quartz sample. Since the sand used in our measurements is comprised mainly of silicates, it is safe to assume that the quartz values will offer a close approximation to those for our contaminant.

For particles that are large ($\gg 250$ μm) reflectance is low and absorptions are moderate. As the particle size decreases, the reflectance increases as the number of
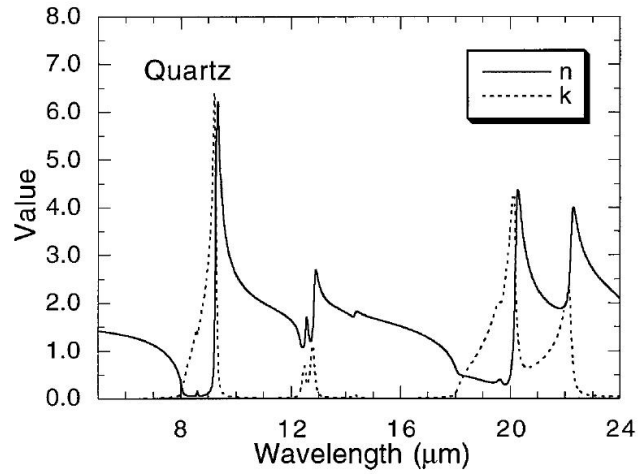
Figure 5.7: The real (n, dashdot line) and imaginary (k, solid line) parts of the complex index of refraction for quartz [Mustard and Hays (1997)]

first-surface reflections and the amount of multiple scattering increases. The absorption strength initially increases with decreasing particle size up to a point where the mean optical path length and the absorption path length ($\sim \lambda/4\pi k$) are comparable. Beyond that point, any decrease in particle size results in a weakening of the absorptions. This is referred to as Class 3 [Moersch and Christensen (1995)].

Restrahlen bands occur when $k > 0.1$. Very little energy passes through the grain boundaries and the scattering and absorption properties are controlled by first surface reflectance and multiple scattering. At this point, the reflectance is at a maximum and the emissivity at a minimum. For large particles, there is little multiple scattering and reflectance is at a maximum. As the particle size decreases to less than the wavelength, the particle as a whole interacts with a wavelength of light. The decrease in scattering efficiency is proportional to $1/\lambda^4$ while the decrease in absorption efficiency is proportional to $1/\lambda$. This is referred to as Class 1 [Moersch and Christensen (1995)].

Traditionally, the Christiansen feature may be defined as the spectral feature that

occurs when $n = 1$ and k is small. At this point there is a minimum in reflectance and a maximum in emissivity. Hapke (1993) distinguishes between the Christiansen wavelength where $n = 1$ and the emissivity maximum described as the Christiansen feature. The Christiansen feature is displaced to longer wavelengths than the Christiansen wavelength and is located where particle scattering undergoes a transition from volume-scattering to surface-scattering.

For completeness, where k is in between that for Class 1 and Class 3, Class 1 behaviour initially dominates as grain size decreases. At some size, the grains become sufficiently transparent that Class 3 behaviour dominates. This means that the emitted energy initially increases with decreasing particle size and then eventually decreases with a continued decrease in particle size. Appropriately, this is Type II behaviour.

Using the above-mentioned classes and the values for n and k, we can estimate where to expect the restrahlen bands and Christiansen features. k is large (> 0.1) around 9 and 13 μm. k has the greatest magnitude around 9 μm and this the anticipated location of the restrahlen bands. The Christiansen feature occurs when $n=1$ and k is small. For quartz, this should occur close to 7.5 μm. These theoretical locations will be used in the analysis of our results.

Although we have developed the mathematical expressions needed to understand the theory, we will not continue with this approach for our data analysis. Instead, the broader concepts presented by this theory will be used. Concepts such as the effect of particle size, optical depth, layer thickness and the relationship between reflectance and emissivity are all very important in determining the approach used for this research. They will also provide the foundation for our analysis of the results.

5.7 Water Theory

Most work done on water concentrates on large bodies of water such as lakes or coastal regions. While this is not what we are interested in, we can use some of the fundamental theory to understand how we might approach the work for thin layers of water. When making measurements in natural settings (lakes, oceans, bogs, etc), we need to take into account various constituents and impurities. In the laboratory, we are better able to control our water source and, as such, we are not concerned with contaminants or suspended sediments. The surface roughness, for larger bodies of water, is a concern when making reflectance measurements. Due to the scale of our work, however, we did not need to take this into consideration. In terms of solar energy, more energy is reflected from water surfaces at low sun elevation angles than at high angles. Solar energy that is not specularly reflected is refracted downward at the water surface and is affected by absorption and scattering. The amount of absorption and backscatter from a body of water are highly dependent on the wavelength interval being measured.

A clear and shallow body of water will have solar energy from the bottom that is reflected and detected by the instrument. This means that the thin layers of water that we are interested in will have a component that is the result of the background material. The penetration of radiation into pure water is described by the extinction coefficient, κ. It takes into account the absorption and scattering effects. The intensity of a parallel beam of radiation of wavelength λ passing through a distance dx is reduced by an amount dI. The reduction is proportional to the intensity, the distance and the extinction coefficient.

$$dI = -\kappa I dx \qquad (5.28)$$

If the intensity at $x = 0$ is I_0, then for some distance x, $I = I_0 e^{-\kappa x}$. Figure 5.8

shows the values of κ ranging from $\lambda = 0.186$ to $2.65\,\mu m$. These values are only valid for pure water.
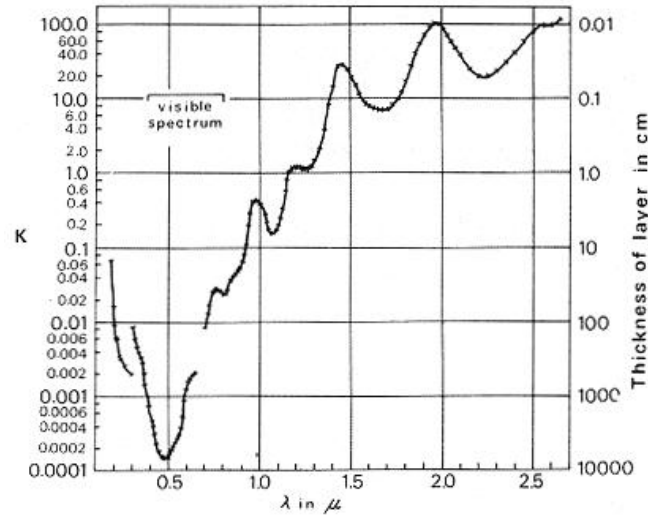
Figure 5.8: Absorption coefficients $[cm^{-1}]$ for pure water as a function of wavelength [Figure 29-27, Salomonson (1983)]

Although bodies of water are highly transmissive in the visible and near-infrared (VNIR) regions, nearly all incident energy is absorbed in the shortwave-infrared (SWIR) portion of the spectrum. Very little energy is back-scattered in this region and, as a result, water tends to have a significantly lower reflectance than terrestrial features in this portion of the spectrum. Curve d in Figure 5.9 shows how the reflectance drops off to zero for Case 1 waters, which are loosely defined as deep-ocean waters. This figure will be of importance later when we are analyzing our results. It is important to note at this time that although we are not dealing with Case 1 or Case 2 waters in our experiments, the underlying theory and phenomenology of water still applies.

In all water measurements, it is important to understand the role that the bottom layer, in our case the different materials, may have on the spectral reflectance. In the
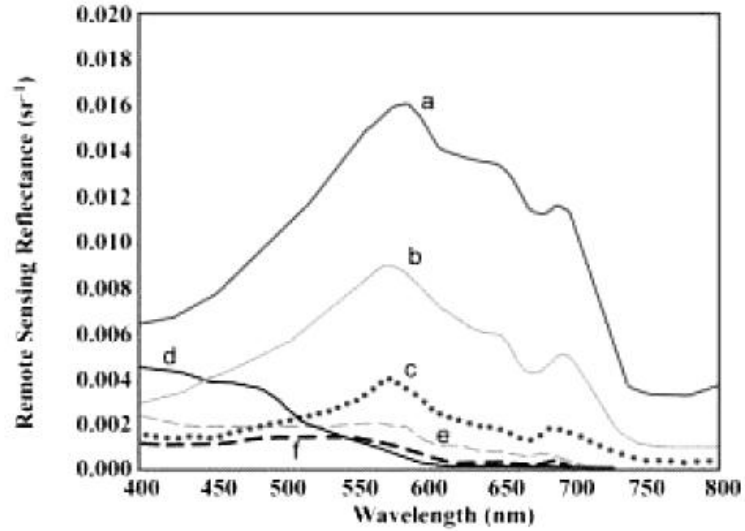
Figure 5.9: Some examples of remote sensing reflectance spectra $[\text{s}r^{-1}]$ from different types of waters. Curve d is an example of clear water (Case 1 water) [IOCCG (2000)]

clearest waters, the bottom is detectable up to a depth of 20-30 m [IOCCG (2000)] in the visible part of the optical spectrum. This is intuitive for most and is very important in our measurements. Since we are only concerned with very thin layers of water, we will always be able to see the bottom and it will always have an influence on the resulting measured spectrum.

This theory is applicable to all of the work that will be done in the field and the laboratory setting. With the knowledge that radiation is highly absorbed in the SWIR, we will need to pay particular attention to this region. As well, the layer thickness will be a major concern since the intensity of the radiation is greatly reduced by even very thin layers.

5.8 DIRSIG Theory

The name DIRSIG is an acronym for Digital Imaging and Remote Sensing Image Generation. The first part of the formal name comes from the Digital Imaging and Remote Sensing (DIRS) Laboratory at the Rochester Institute of Technology (RIT) where the model was created. The information in this section and further details may be found at `http://www.dirsig.org`.

The reflectance of a material's surface has been shown to be a function of wavelength, illumination angle, and view angle. The bi-directional reflectance distribution function (BRDF) describes these geometry specific reflectance values for all combinations of illumination and observation angles as a function of wavelength. In the thermal region of the spectrum, many materials take on more specular characteristics (especially at low view angles), therefore correct determination of the background in the specular direction is necessary.

DIRSIG allows the user to include a unique spectral reflectance data set for each material in a scene. To correctly incorporate the specular and diffuse background contributions, DIRSIG casts approximately 100 rays into the hemisphere above the hit point to include radiances from sky and background sources. The radiances identified by each of these rays are then weighted by their geometry specific reflectances.

It is possible to create new scenes and new materials within DIRSIG. Although the specific programming required will not be discussed in this section, we will introduce the parameters that are required in order to do so. In the DIRSIG world, everything is assigned a material. A material is the central method that is used to assign both optical and thermal properties to an element in the DIRSIG world. Therefore, understanding how materials are managed, where they are defined, how they can be defined, etc. is an important aspect to understanding the DIRSIG model.

The optical properties of a material are the driving force in the DIRSIG radiative transfer process. At this time, the model supports three primary types of materials: opaque (non-transmissive), plate-style transmission, and volume-style transmissive materials. We are interested in the opaque materials. The assignment of materials to elements in the scene is part of the scene construction process. To summarize, the object geometry files that the DIRSIG model loads contain geometry elements (usually facets) that were each assigned a material ID number. This material ID number is a reference to a material description in the material database file. Several parameters, including spectral emissivity, specific heat, thermal conductivity, thickness, solar absorptivity, and specularity, are defined and stored in a materials database. This information is then used to create the surface properties when a specific material is applied.

Chapter 6

Instruments & Measurement Techniques

When spectral measurements are made, practical considerations lead to a focus on one part of the spectrum over another. While this is helpful in understanding that region, it is also desirable to be able to look at a full spectrum measurement to get a complete picture. Our research is interested in the full spectrum, 0.350 to 25 μm. This task is ambitious and not without difficulties. For the purpose of discussion, the spectrum of interest will be divided into two categories: 0.350 to 2.5 μm and 2 to 25 μm. The former is what is commonly referred to as the reflective region and encompasses the Visible, Near-Infrared and Short-Wave Infrared (VNIR/SWIR) regions. The latter is known as Mid-Wave Infrared (MWIR) and Long-Wave Infrared (LWIR) regions and is typically referred to as the emissive portion of the spectrum.

6.1   Reflective Region

The reflective region is named so because it is dominated by radiance reflected from a target and its background. Self-emitted radiance, while very important in the MWIR and LWIR regions, is not of concern in the reflective region. Reflected solar and self-emitted energy contribute equally to detected radiance between 3.5 and 4.2 μm, well beyond the reflective portion of the spectrum. This is why, when making measurements with the ASD, we are not interested in the temperature of the materials being measured. Simply, it does not matter for the reflective region. In order to define spectral reflectance at the sensor, we need to look at the factors that contribute to it.

The following equation describes the various factors that make up the radiance measured by a detector.

$$L_S(\lambda) = [L_{direct}(\lambda)\rho(\lambda) + L_D(\lambda)\rho(\lambda) + L_{BG}(\lambda)\rho(\lambda) + L_{albedo}(\lambda)]\tau(\lambda) + L_u(\lambda) \quad (6.1)$$

where:

$L_S(\lambda)$	is the spectral radiance measured by the sensor looking at the target,
$L_{direct}(\lambda)$	is the direct spectral solar radiance onto the target,
$L_D(\lambda)$	is the scattered downwelling spectral radiance onto the target,
$L_{BG}(\lambda)$	is the cumulative spectral radiance from background materials onto the target,
$L_{albedo}(\lambda)$	is the cumulative spectral radiance reflected off background materials, not onto the target,
$L_u(\lambda)$	is the scattered upwelling spectral radiance reaching the sensor,
$\rho(\lambda)$	is the spectral reflectance of the target, and
$\tau(\lambda)$	is the spectral transmission along the path from the target to the sensor.

In order to determine the spectral reflectance of the target using (6.1), it would be necessary to measure each of the radiance terms within the brackets individually. This is obviously not practical and, therefore, we require another set of measurements. The

first required measurement is made using a spectrally flat, calibrated, 100% reflectance standard. The radiance of the calibrated target may defined by an equation similar to (6.1).

$$
\begin{aligned}
L_{S,reference}(\lambda) = [L_{direct}(\lambda)\rho_{reference}(\lambda) + L_D(\lambda)\rho_{reference}(\lambda) \\
+ L_{BG}(\lambda)\rho_{reference} + L_{albedo}(\lambda)]\tau(\lambda) + L_u(\lambda)
\end{aligned}
\tag{6.2}
$$

The only difference between (6.1) and (6.2) is the reflectance term. $\rho_{reference}(\lambda)$ in (6.2) is the spectral reflectance of the reference standard. The spectral radiance reaching the sensor from the target is L_S and that of the reflectance standard is $L_{S,reference}$.

The aim of these measurements is to obtain the spectral reflectance of the target. By looking at (6.1) and (6.2), one can see that they are very similar and several of the terms may be eliminated. The spectral transmission is approximately equal to one because the distance between the target and the ASD is kept to a minimum. Likewise, the small amount of atmosphere that is in between the sensor and the target means that the upwelling radiance, $L_u(\lambda)$, equals zero. The $L_{albedo}(\lambda)$ in this case is assumed to be negligible. By ratioing the radiance of the target to that of the reference standard, we are left with the following:

$$
\frac{L_{S,reflected}}{L_{S,reflected,reference}} = \frac{\rho(\lambda)[L_{direct}(\lambda) + L_D(\lambda) + L_{BG}(\lambda)]}{\rho_{reference}(\lambda)[L_{direct}(\lambda) + L_D(\lambda) + L_{BG}(\lambda)]}
\tag{6.3}
$$

When the two measurements are made close together in time, the direct, downwelling, and background radiance terms may be assumed to be identical. Therefore, it is possible to further simplify (6.3) in order to obtain the reflectance of the target.

$$
\rho(\lambda) = \frac{L_{S,reflected}}{L_{S,reference,reflected}}\rho_{reference}(\lambda)
\tag{6.4}
$$

(6.4) is only true when the above-mentioned conditions are met. It is therefore important that sky conditions be monitored as well as the position of background objects in order to keep the error level to a minimum. A key component to this equation is the reflectance of the reference standard. In an ideal world, one would use a pristine piece of white Spectralon [`www.labsphere.com`] as the reference standard. Spectralon gives the highest diffuse reflectance of any known material or coating over the UV/VNIR region of the spectrum. The reflectance is generally $> 99\%$ over a range from 400 nm to 1500 nm and $> 95\%$ from 250 nm to 2500 nm. For this reason, a pristine piece would offer a value close to unity for $\rho_{reference}(\lambda)$ and it could be eliminated from the calculation. In the real-world and in our measurements, the sample was not quite pristine. In order to achieve NIST-traceable reflectance values for out materials, a correction factor for our standard should be calculated. This could be done by ratioing the spectral reflectances of our standard and a pristine sample of Spectralon. This calibration factor was not calculated for our research.

This theory outlines the basic procedure used when measuring the reflectance with the Analytical Spectral Devices (ASD) FieldSpec Pro Spectroradiometer. The ASD employs three separate spectrometers to cover the 0.350 to 2.50 μm range. The visible and near-infrared regions (0.35 to 1.0 μm) are measured with a fixed concave holographic reflective grating and a linear photodiode array. The two SWIR (1.0 to 2.5 μm) spectrometers use scanning concave holographic reflective gratings and fixed In-GaAs detectors. It is a single beam spectroradiometer, and its operation reflects the nature of this design [DIRS Lab (2003)].

The primary advantage to making measurements in the reflective region is that, unlike the emissive portion of the spectrum, it is not sensitive to temperature changes. This means that less care needs to be taken to control the environment insofar as the

surface or air temperature. There are, however, significant water absorption bands in the region that prohibit any valuable data from being collected within them. These two bands are at 1.45 and 1.95 μm, respectively. As the solar irradiance travels all the way through the atmosphere to the target, it must pass through a significant amount of water vapour. As such, the irradiance in these bands is very low and the incident irradiance approaches zero. This causes instability in the reflectance calculation. Since the atmosphere is rarely dry enough to make it possible to obtain useful data in these bands, the spectral regions within them are simply ignored. These regions are not of significant concern when measurements are made in the laboratory. Although additional absorption features due to water, hydroxyl and iron are also present within this range, they are not as prominent and will not be discussed further.

6.2 Emissive Region

The following theoretical discussion applies to measurements made in the thermal regions, including the MWIR and LWIR, of the spectrum. It is also the governing theory behind the use of the D&P Instruments 102F FTIR Spectrometer (D&P) which allows for measurements over the second region of interest, 2 to 25 μm. The core of the spectrometer is the Michelson interferometer. This contains infrared optics, beam splitter, and a scanning mirror assembly. Input light passes through the fore optics, an aperture, and a lens into the interferometer. The output light passes through a focusing lens onto an infrared detector in a liquid nitrogen (LN_2) dewar. The standard detector is a dual sandwich type, consisting of Indium Antimonide (InSb) over Mercury Cadmium Telluride (HgCdTe, or MCT) [D&P Instruments (2004)].

The theory for MWIR and LWIR radiation is perhaps a little less intuitive than that presented for the VNIR/SWIR region. As previously mentioned, reflected solar

and self-emitted energy contribute equally to detected radiance between 3.5 and 4.2 μm. The spectrum beyond 4.2 μm is dominated by the self-emitted term but may still have a significant reflected component. Targets with smooth surfaces that are viewed at or near the specular reflection angle for the sun will contain a significant reflected component. Dominance of reflectance in this region is also likely to occur when the temperature of the target is not significantly warmer than the background. In situations other than these, the self-emission term dominates the radiance field. This is especially true beyond the CO_2 absorption band at 4.4 μm.

As in the reflected part of the spectrum, it is important to recognize that background materials and the atmosphere play a significant role in the overall radiance due to reflection and scattering, respectively. These elements also introduce additional energy into the radiance field due to their kinetic temperature. Large aerosols and clouds are very important contributors to the overall energy in the scene as well. These tend to act as blackbody emitters and can greatly vary the background radiance. Once again, measurement geometry and time of acquisition are crucial to obtaining reliable data. Other factors that greatly influence the radiance field in this region are the solar loading and wind speed. Both of these can greatly affect the surface temperature of the target. The wind can cool the surface of a material very quickly and, since it is the surface layer that is responsible for the majority of the infrared emission, changing temperatures will result in a poor determination of the emissivity.

The mathematical description of the radiance received by a sensor in this spectral region is:

$$L(\lambda) = \tau(\lambda)[\epsilon(\lambda)L_{BB}(T_S, \lambda) + (1 - \epsilon(\lambda))L_D(\lambda)] + L_u(\lambda) \qquad (6.5)$$

where:

T_S	is the target surface temperature,
$\epsilon(\lambda)$	is the spectral emissivity,
$\tau(\lambda)$	is the to-sensor spectral atmospheric transmission,
$L_{BB}(T_S, \lambda)$	is the spectral blackbody radiance at a target surface temperature T_S,
$L_D(\lambda)$	is the downwelling radiance, and
$L_u(\lambda)$	is the upwelling scattered and self-emitted path radiance

Ultimately, we are interest in calculating the emissivity of the material-contaminant combinations. By rearranging **??**, we can obtain an equation that describes the emissivity of a material in terms of the sample, downwelled and blackbody radiances.

$$\epsilon(\lambda) = \frac{L(\lambda) - L_D(\lambda)}{L_{BB}(T_S, \lambda) - L_D(\lambda)} \tag{6.6}$$

The transmission term, $\tau(\lambda)$, is equal to one because the distance between the instrument and the material is minimal and the upwelling radiance is considered negligible over this path distance.

In order to measure the radiance, it is necessary to make measurements that are both time effective and useful in a real-world scenario. The simplest of these is to measure the downwelled radiance onto a reflector. The radiance field leaving this plate, when it is placed at the same position and orientation as the target, may be measured and compensated for its own self-emitted component. Depending on the plate material, the temperature and spectral emissivity of the plate must be well-known in order for this measurement to be done accurately.

An inexpensive and very effective way of creating a standard for use in the field is to use crinkled, heavy-duty aluminium foil placed over a stiff cardboard panel. Crinkling the aluminium foil creates random orientation to the surface and is a good approximation to a diffuse surface. This means that the plate is not as sensitive to viewing

angle when making radiance measurements. Aluminium foil has a low density and thermal inertia that allow it to quickly change temperature and remain close to the ambient air temperature. This has both advantages and disadvantages. Care must be taken not to shadow the surface of the plate while taking temperature measurements since the surface will cool rapidly. This material has a low emissivity/high reflectivity nature which results in a very low magnitude radiance field to measure. This in turn results in reduced measurement accuracy. In this case, it is not necessary to know the temperature of the surface very accurately since the self-emitted portion of the signal is very small ($\epsilon \ll 1$). This advantage, and the fact that it is easily replaceable if it is damaged, make the aluminium foil plate the best choice for measurements made in the field.

Another method is to use a diffuse gold standard plate, such as the InfraGold plate from Labsphere. In order to avoid collecting measurements at the specularly reflected angle, the viewing geometry of the plate, which is not entirely diffuse, must be considered. Due to the ease with which this surface is contaminated, its cost and the need to measure its temperature accurately, this standard is best suited for lab use. Both the gold and the aluminium have shown similar performance levels.

6.3 Field Measurements

The theoretical discussion above explained how measurements were made when using instruments that cover the reflective and emissive regions of the spectrum. The ASD and D&P were both used in the field to make measurements of vehicles and asphalt with a variety of surface conditions. The ASD and D&P were used separately when the asphalt measurements were made and did not require any special set-up. In order to measure the same spot on the vehicles at the same time with both instruments,

we created a set-up that put both of the instruments on a single tripod. In order to accomplish this for the vehicle measurements, the set-up shown in Figure 6.1 was used:

Figure 6.1: Vehicle measurement set-up (red circle indicates the location of the instruments)

Procedurally, the measurements were made in accordance with the guidelines and protocols for each instrument.

6.4 Laboratory Measurements

The above-mentioned theory also applies to making measurements in the laboratory. However, there were certain key factors that did need to be considered and the instrument set-ups needed to be modified to take them into consideration. Two major factors were the lack of thermal contrast in the laboratory and the lack of natural and powerful illumination from the sun. In order to use these instruments in the laboratory, it was necessary to create a set-up that would compensate for these missing components. We were also able to make use of the controlled laboratory setting to improve upon some

of the set-up normally used in the field.

The D&P requires that there be a thermal contrast between the measured surface material and the sky such that the radiance values for each, L and L_D respectively, are significantly different. Clearly, (6.6) would not have a solution if these values were the same. In the field, this difference is naturally present because materials on the ground are generally warmer than the sky. In the lab, however, this thermal contrast is not as significant. In order to achieve this contrast, we made a false sky in the lab by filling trays with ice (see Figure 6.2). Setting the D&P in the centre of these trays allowed the "sky" to appear semi-infinite to the instrument and the material being measured. Next, we heated the sample materials to further increase the temperature difference between the two surfaces. In most cases, this difference could be maintained at about 30℃ or greater. In fact, is was necessary for us to maintain a difference of at least this amount in order for post-processing techniques to work properly. Only two of these techniques could be used: blackbody fit [A. Kahle and R. Alley (NASA JPL, 1992)] and known sample temperature. Both techniques yielded similar results. The first of these fits a Planckian radiation curve to the entire measured sample radiance by assigning the highest temperature value which will not allow the spectral emissivity to exceed the specified maximum emissivity over a wavelength region. The latter method uses the measured temperature of the sample to create a Planckian curve. If the measured temperature of the surface is not known or has not been measured accurately, then the known sample temperature method should not be used. Other techniques also exist but were not used in this research.

During the course of our laboratory measurements, we encountered an issue with the values in the MWIR region that made us question their accuracy. Upon comparison with the standard calibration files, we noticed a significant difference in magnitude of
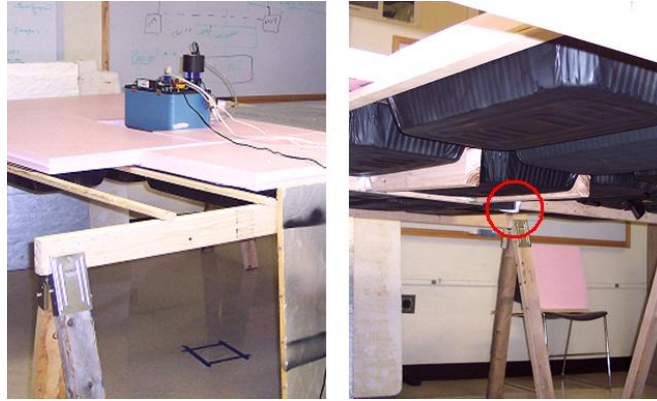
Figure 6.2: Laboratory set-up for the D&P (the red circle indicates where the viewing port for the D&P was situated among the trays)

the raw instrument counts between the calibration files and our laboratory measurements, indicating a loss in sensitivity of the InSb detector. Our conclusion was that there was a problem with the D&P and the MWIR data were unreliable. As a result, only the LWIR measurements will be analyzed for this report.

The ASD is far more forgiving when moving into the lab because the VNIR/SWIR regions are not as sensitive to temperature changes. It does, however, require that the surface be illuminated with a constant and steady source. Outdoors, the sun takes care of the this. When we moved into the laboratory, it was necessary for us to create a replacement for the sun. We found, through trial an error, that a couple of high powered flashlights had enough intensity to illuminate the surfaces adequately. It is necessary that they run off a DC power supply so that additional AC noise is not introduced into the system.

The ASD has a field of view (FOV) made up of many smaller fields of view. The individual smaller FOVs are created by the optical fibres that are each associated with only one of the three detectors (VNIR, SWIR1 and SWIR2). Since they each have a physical size, do not overlap with one another and are not randomly distributed, dis-
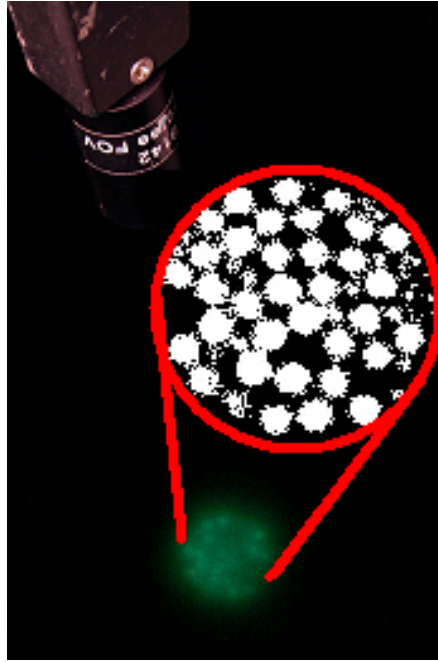
Figure 6.3: ASD FOV, with smaller FOVs for each of the detector optical fibres

continuities in the measured spectra often occur (Figure 6.3). More often than not, the discontinuities occur when the material being measured has some non-uniformity to it. This has been noted when making measurements of materials such as grass. In our case, asphalt and concrete have definite non-uniformities and the situation is exacerbated by putting sand on each of these materials. The simplest way to reduce or eliminate these discontinuities is to rotate the sample underneath the FOV of the ASD probe, thereby creating several spectra over which we could take an average measurement. Over one rotation, the ASD made 10 measurements and each of these measurements consisted of 30 averaged spectra. This technique allowed us to average out the discontinuities while maintaining the integrity of the sample and of the measurement itself. This was accomplished by placing the sample on a potter's wheel and rotating it. The ASD laboratory set-up is shown in Figure 6.4. It is obvious why this would not be practical

to do in the field.
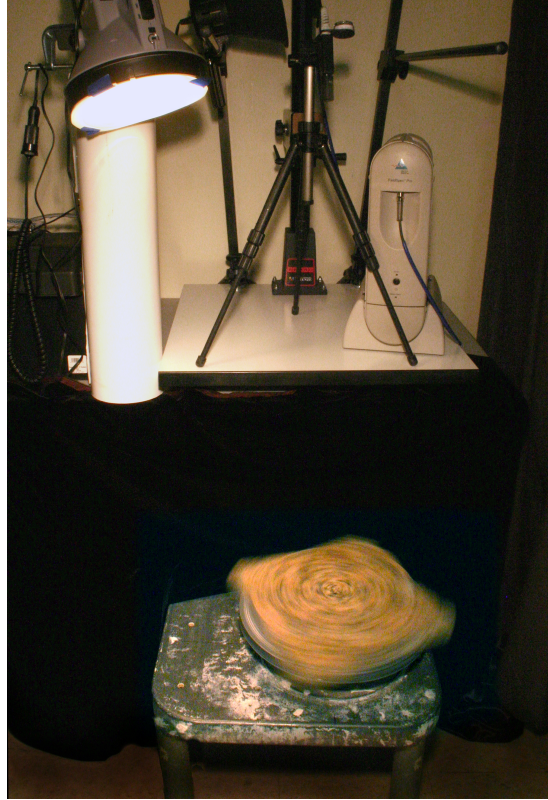
Figure 6.4: Laboratory set-up of the ASD

As previously mentioned, only the concrete and asphalt were measured with both of the contaminants. The reason for this is easy to see in Figure 6.4. The smooth surface of the painted metal and the relatively smooth roofing shingle could not contain the water within the FOV of the instrument. An accumulation of water on each of these surfaces was not possible and therefore these two materials were measured only with the sand as a contaminant.

6.5 Modular Imaging Spectrometer Instrument (MISI)

MISI was used to capture aerial images of the campus for later use in the validation of our results. In order to understand what MISI is, the following is a brief introduction to the instrument. This and additional information may be found at `http://dirs.cis.rit.edu/research/misi.html`. The Digital Imaging and Remote Sensing Laboratory at RIT constructed an airborne imaging spectrometer called MISI. It is a line scanner with a 6" rotating mirror coupled to a Cassegrain telescope of focal ratio f/3.3. Two 0.5 mm square silicon detectors (broad-band visible) and two 1.5 mm fibre optics are placed at the primary focal plane to give a GIFOV of 0.3 m and 1.0 m respectively at 0.3 km of altitude. At a typical flying height of 2500 ft, the GIFOVs are approximately 0.75 m and 2.5 m. The two 1.5 mm fibres lead to two separate 36-channel spectrometers to cover the EM spectrum from 0.440 μm to 1.020 μm in 0.010 μm spectral bands.

Chapter 7

Results

7.1 Qualitative Results

The field measurements were made to provide us with a set of preliminary results and a qualitative understanding of the phenomenology. We measured vehicles with a variety of surface conditions and asphalt with our sand contaminant. Before we review the results of the field measurements, we will briefly describe of the particle size distribution, layer thickness and moisture content along with the materials of interest.

7.1.1 Preliminary Discussion

7.1.1.1 Particle size, layer thickness, moisture content

We made our own particle size separate by sieving the largest and smallest particles out of our sand sample. The largest particles were removed so that the scattering characteristics would be from closely packed particles and the smallest ones, known to increase overall reflectance, were removed as well. Although the particle size distribution in this work was still quite broad, we felt that it represented a reasonable sample

that could be found outdoors. Limiting the size separate further would be more useful from a theoretical standpoint and but less practical in a real-world simulation. We are only concerned with the layer thickness of the sand insofar as it pertains to the optical depth. Once we know how thick the layer of sand needs to be to be considered optically opaque, any other concern over the layer thickness is moot. Although we did make measurements of water on the samples, we were not interested in measuring the effect of water and soil combined on the spectral reflectance. The moisture level of the soil will be kept to a minimum and therefore relatively consistent over all of our measurements.

7.1.1.2   Materials

In all cases, the surfaces were dry and clean at the beginning of each set of measurements.
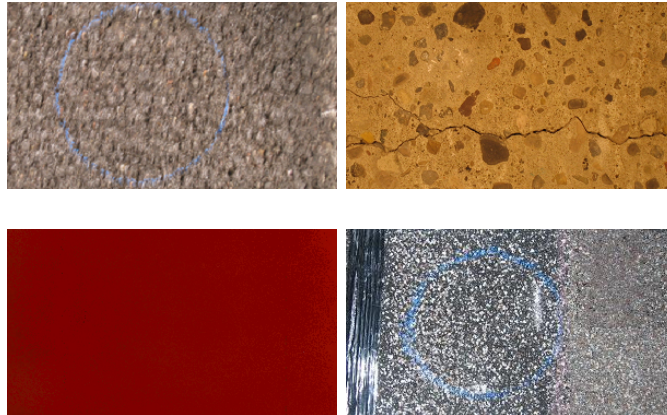

Figure 7.1: Material samples: asphalt, concrete (top); painted metal, roofing shingle
Scale: Image height is ~ 4 inches

The asphalt and concrete samples were prepared for the measurements lab and are representative of concrete that one would find on most roads and sidewalks, respectively.

Each of these samples were encased in a wooden frame. The painted metal is an aluminium sample painted red. The paint is not entirely diffuse but does not appear to have a reflective coating. The final sample is a roofing shingle. It is a standard tar roofing shingle, used mainly in residential construction. Sample images of each of the surfaces are shown in Figure 7.1.

7.1.2 Vehicles

As targets of convenience, we chose to measure vehicles with a variety of surface conditions for our first set of qualitative measurements. These were convenient targets for several reasons. First, by using vehicles that belong to people within the Center for Imaging Science, they were readily available. Second, all vehicles were measured as they came to us: dirty. This meant that we did not need to add any soil to the surfaces. Third, since we built our own set-up to allow for overhead measurement of the vehicles, we were able to chose a location that was further away from other vehicles, buildings and general traffic. By minimizing the background clutter and movement the measurements would also be more accurate.

Once the set-up was ready, each vehicle was measured with four surface conditions. The vehicles were measured as they came to us: dirty from city and highway driving. This allowed us make some measurements of soiled surfaces without any quantification of the amount of dirt, the particle size or type of dirt. We measured a series of vehicles for this research. Table 7.1 summarizes the measurements that were made and Appendix D contains the bulk of these results.

We began with the car dirty and dry, then added water to the surface to get a dirty and wet spectrum. Cleaning the surface off gave us a clean (relatively clean compared to the initial dirty surface) and dry condition. Finally, we saturated the surface and

Vehicle	ASD:				D&P:			
	dd	dc	wd	wc	dd	dc	wd	wc
Green, Subaru*	x	x	x	x	x	x	x	x
Green, VW		x		x	x	x	x	x
Green, BMW	x	x	x	x	x	x	x	x
Blue, Mustang	x	x	x	x	x	x	x	x
Blue, Focus*	x	x	x		x	x	x	
White, Saturn*	x	x	x	x	x	x	x	x
Black, BMW	x	x	x		x	x	x	x

Table 7.1: Vehicle measurements, with four different surface conditions:
dd - dry, dirty, dc - dry, clean, wd - wet, dirty, wc - wet, clean. More detail of the
set-up and the surface conditions for the vehicles marked with an asterisk (*) is given
in Appendix D

measured it in a clean and wet state (Figure 7.2). The saturated surface may have had beaded water on it or a thin film of water. The degree to which either of these occurred was dependent on the amount of wax or other contaminants on the surface. These four straight-forward measurements gave us a look at how soil and water on a surface could affect the spectra.

The data for the emissive portion of the spectrum is only shown between 8 and 14 μm. Because of various absorption spectra and their influence on the thermal portion of the spectra, most other areas do not provide useful information. For the MWIR, we could plot the results from 3-5 μm, however only the data between 4.6-5 μm is free from strong absorption bands. As such, we left this analysis to the measurements in the laboratory. In Figure 7.3, the relationships between the different surface conditions can be seen.

Looking at each of the different regions, the following analysis was done. Over the VNIR region, the dry and wet spectra, respectively, are nearly identical. At the transition around 1000 nm, there is a change that occurs and, instead of the amount

Figure 7.2: Images of Subaru measurements - top: vehicle set-up, bottom left: dry and dirty, bottom right: wet and dirty

of moisture on the surface, the amount of dirt on the surface becomes the determining factor for similarity. The clean and dirty spectra, respectively, are most similar over the 1000-1500 nm range. After the strong water vapour absorption feature at 1400 nm, the dry spectra are most similar in shape and have generally higher reflectance values than the wet spectra. The clean and dry spectrum continues to have a higher reflectance value than the dry and dirty curve. The only real difference between these two spectra is in the magnitude and not the shape. This trend continues to the end of the ASD measurement range at 2500 nm. For the wet surface conditions, at wavelengths greater than 2000 nm, the spectra are almost identical. Between the water vapour absorption features at 1400 and 1900 nm, however, the wet and clean spectrum has a larger increase in reflectance than the wet and dirty spectrum. This trend is similar to the lower end of the SWIR region. Once again, the soil coverage from the dirty surface plays an
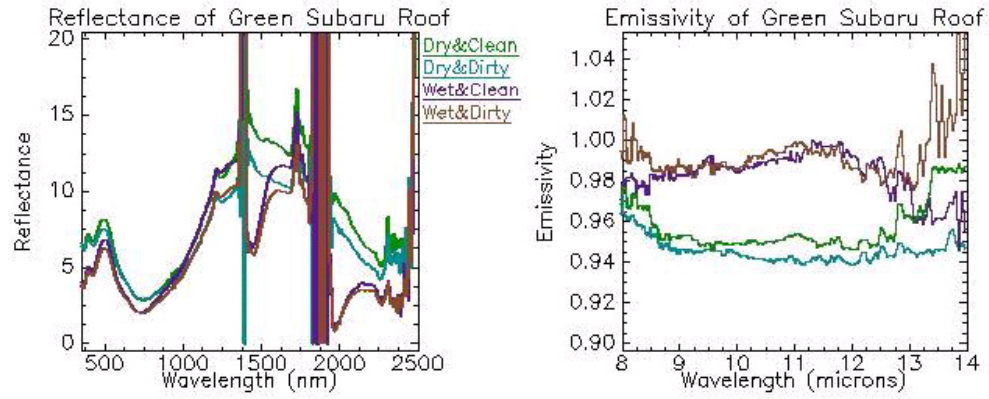
Figure 7.3: Plots of Subaru spectra - ASD data (left), D&P data (right)

important role in the overall reflectance of the surface.

Over the 8-14 μm range, we can see that the wet spectra generally have higher emissivities. This is expected since a thick layer of water is 100% emissive. Given that the amount of water on the surface was not considerable in depth, this indicated that in order to capture variation in the coverage amount, the water would have to be added in small increments to the surface. The 100% emissivity mark was not attained because the layer was not uniform and the water formed droplets on the painted surface. In this region, the greatest influence on the overall emissivity is the amount of water on the surface. The dirty surfaces do show some slightly different emissivity values, but this change is not as great as that created by the water.

Other features that are seen in these spectra, and others to follow, are the water vapour absorption features around 1.4 and 1.95 μm. These water absorption features are characteristic of all measurements made in the field due to the atmospheric water content. These features, however, are not as broad as what is seen in the plots. It is very difficult to isolate only the feature itself when making outdoor measurements even with frequent optimization and calibration of the instruments. The humidity levels

in Rochester, NY tend to be high in the summertime and as such the water features are affected. In a more arid environment, the features would be better defined. The hydroxyl feature around 2.25 μm is also visible in most of the plots, although the exact location does vary somewhat. Liquid water absorption features are easily seen at 1500 and 2000 nm.

7.1.3 Asphalt

To extend our qualitative understanding of the effect of the contaminants on a surface that is predominant in many urban scenes, we chose to make measurements of the contaminants on our asphalt sample. Although these measurements we not exactly quantitative, we did place a little bit more control on the surface conditions than we did with the vehicles. Measurements were made for both sand and water as contaminants.

We made two sets of measurements with sand on the asphalt. First, we compared the reflectance of optically thick piles of different size separates of sand to previously published data. Second, we incrementally increased the layer thickness of the sand from no coverage to beyond the optical depth. The theory section detailed that once the optical depth of the top layer, sand in our case, was achieved the reflectance spectrum would equal that of the top layer. Therefore, when the reflectance/emissivity values stopped changing, the layer had reached its optical depth.

For the first set, we needed distinct size separates. The sand used was sieved into three different size separates to demonstrate the effect of particle size on the reflectance spectra. The size separates were identified as grades 0, 1 and 2, from coarsest ($>$1 mm) to finest ($\ll$1 mm), respectively. The following plots indicate that the reflectance of smaller particles is greater than that of the larger particles. This is directly in line with the theory previously presented.

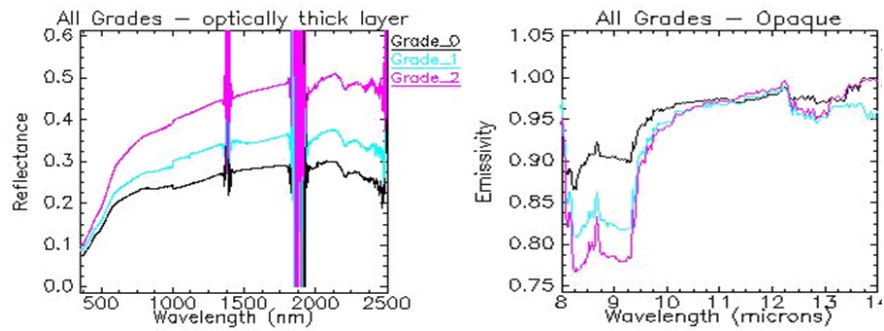Figure 7.4: Sand size separates: coarsest (left) to finest

Figure 7.5: Reflectance plots of different size separates under optically thick conditions

Grade 0 sand has the largest particles and also the lowest reflectance while grade 2 has the smallest particles as well as the highest reflectance. This pattern continues through to the emissive portion. The spectra may appear to be in a different order for the thermal region, however, due to the complementary nature of reflectance and emissivity (Kirchhoff's law), the order is in fact the same. The shape of the curves is also maintained throughout.

We were also able to establish how the spectra change with increasing sand depth. As sand was added to the asphalt surface, an increase in reflectance was obvious. The sand is much lighter in colour than the asphalt and as a result also has a higher reflectance. The more sand on the surface, the less the background reflectance of the

asphalt could be seen. The reflectance increased up to the point where the optical depth of the sand was reached and the reflectance matched that of the sand alone. At this point, the background was completely hidden by the sand. To make things simple, we will only look at the grade 2 sand. The other grades also exhibited the same trends but the separation between the curves was not as great as with grade 2 sand.
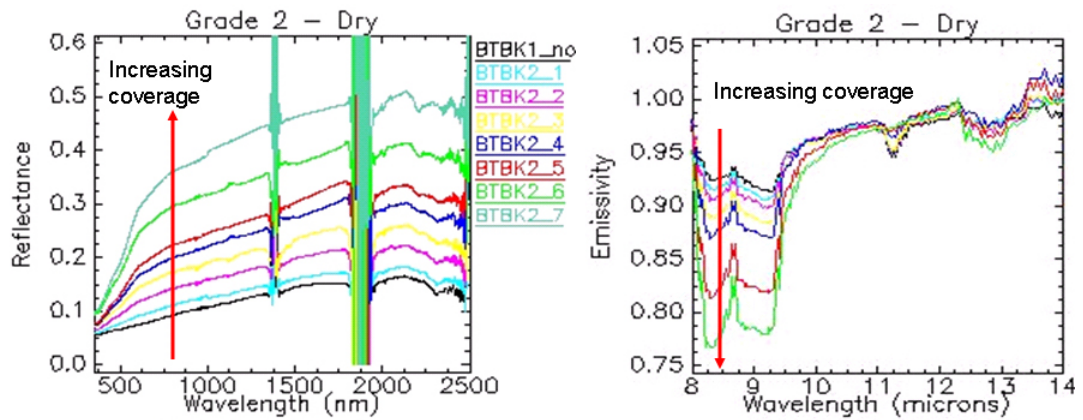

Figure 7.6: Spectral reflectance and emissivity of grade 2 sand (increasing thickness in the direction of the arrows)

For comparison sake, Figure 7.7 below shows data measured by us (left) and data provided by Salisbury and D'Aria (1992). Even though the magnitude of the reflectance values differ, the curves do have the same general shape. The key quartz features between 8-9.5 μm and 12-13 μm are present in all of our measured results. We can draw a couple of conclusions from this. The first being that we have made measurements of sand that are in-line with previously obtained results and the second is that our sample likely has a high quartz content. While the magnitude of the curves in Figure 7.7 differ, the largest difference between the two plots is that the published results are of a pure quartz sample while the sand that we used was a mixture. The latter point is not much of a stretch since we know that the sand used was largely comprised of silicates.
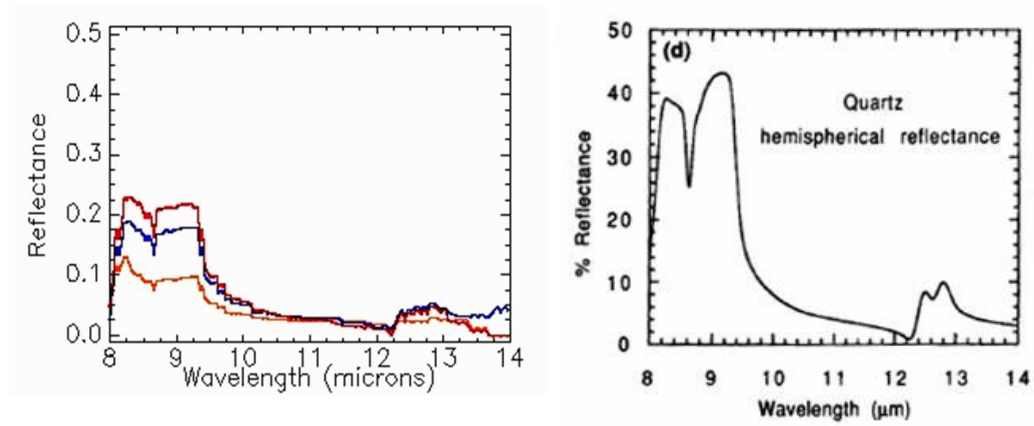
Figure 7.7: Comparison of measured and published results [Salisbury and D'Aria (1992)]

Water on the surface itself did not prove to be a very successful endeavour because of the weather. Ideal sky conditions also meant that the surface of the asphalt was very warm and that the water evaporated fairly quickly from the surface. While it is possible to make measurements at other times, i.e. during the night, it was not practical to do so. We made several measurements of increasing amounts of water on the surface to demonstrate the effect of the amount of water on the reflectance values.
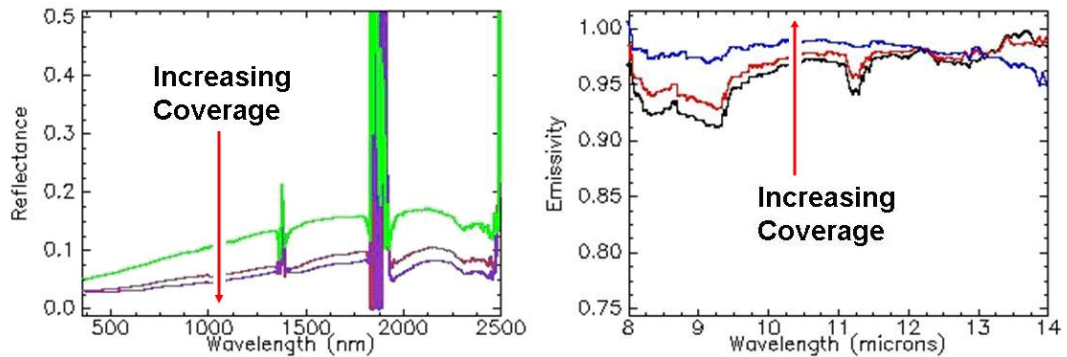

Figure 7.8: Water on asphalt: ASD (left) and D&P

Using the same asphalt sample, we gradually wet the surface until it was completely saturated. As shown in Figure 7.8, the emissivity of the surface increases when water is added to it. The reason why an emissivity of 1 is not achieved has mainly to do with the fact there is some texture to asphalt. We were not able to achieve a uniform layer of water over the entire surface and therefore some of the asphalt, although wet, did not have a uniform layer of water on it.

Another measurement of wet asphalt was made using our airborne sensor, MISI. The plan was to capture consecutive images of the RIT campus. The only difference between these images that we were interested in controlling was an area of the parking lot. This area was dry in the first image and wet in the second. The image in Figure 7.9 provided a truth image against which we could compare our synthetic scene.

Figure 7.9: MISI image of the RIT campus: large puddle is highlighted

This dataset, along with the DIRSIG scene, was used in the modelling of sand and water on asphalt. The modelling and validation results are discussed in the following chapter.

7.2   Quantitative Results

Using the laboratory instrument set-ups described in the Chapter 6, we made a series of measurements combining the different materials and surface contaminants. For analysis of the results, we took a look at each material and contaminant combination. Before we delve into the results, a few items need to be reviewed. A discussion about the assessment of the percentage coverage, the types of relationships that were observed between the reflectance and the percentage coverage at different wavelength intervals, and how the emissivity files were created for use in DIRSIG will allow for a clearer understanding of the steps involved in this analysis.

7.2.1   Preliminary Discussion

7.2.1.1   Percentage coverage assessment

Each of the materials were measured with sand coverage. However, the amount of sand that was dispensed onto the surface each time varied. For this reason, a digital image of each area captured by the instrument FOV was taken. This information could then be used to verify the percentage coverage in each case. It is possible to determine the FOV of each instrument with some basic trigonometry and from data provided by the manufacturer. In both cases, the instrument field of view was approximately 4 inches in diameter. Using this knowledge and images takes during the measurements, we could then use a couple of tools to get an exact calculation of the percentage.

The tools used were Photoshop CS2 and ENVI. The former was used to truncate the image to the FOV and create a threshold image for the image statistics to be computed against. ENVI was used to run a classifier on the image and then compute the statistics of each of the regions. An example of the steps involved in the process may be found

in Appendix A.

7.2.1.2 Functional relationships: reflectance vs. percentage coverage

Using the information retrieved from each of the images, we then plotted the reflectance as a function of the percentage coverage for discrete wavelengths. The wavelength intervals were chosen such that the entire range was covered and that significant features were also included, i.e. quartz doublet between 8 and 9.5 μm. What we found was that the relationships fell into one of two categories: highly linear or quadratic. The cases that were highly linear resulted in simple percentage combinations of the bare material spectrum with the pure contaminant spectrum to obtain a fixed percentage coverage. All materials were linear over the entire thermal region. The reflective region, however, demonstrated that linear combinations were not sufficient to describe the material-contaminant combinations over that region. In this region, most of the relationships could be described by a second-order polynomial. All of these relationships were calculated by using a short IDL program listed in Appendix B. Figure **??** shows the functional relationships for asphalt and sand over the reflective and thermal regions, respectively. Additional plots for the remaining datasets may be found in Appendix E.

7.2.1.3 Emissivity files

The data needed to create the emissivity files for DIRSIG was the output of the IDL program mentioned above. The text files that it created could easily be converted into the appropriate structure for the emissivity files. The emissivity files will accept wavelength-emissivity pairs for any number of wavelengths from 0.35 to 25 microns. To better understand the format of these files, please refer to Appendix C. The first
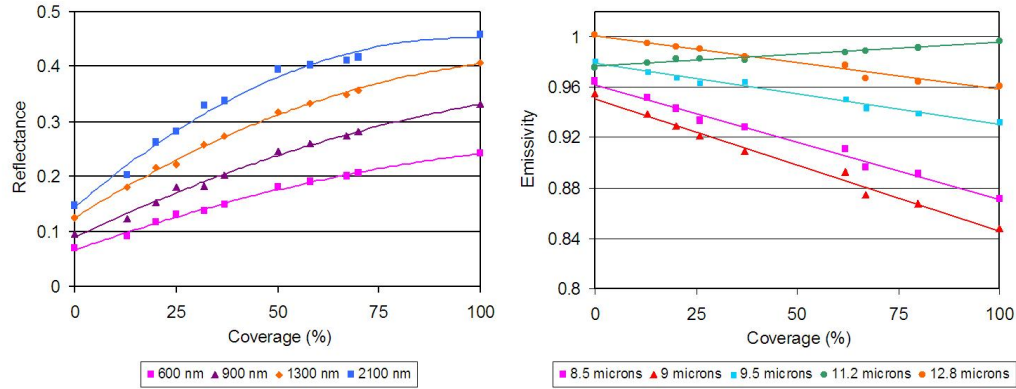
Figure 7.10: Asphalt and sand: non-linear over the reflective region (left) and linear over the emissive region

section of each file contains the information on the number of spectra and the values for the angular weighting function from 0 to 90 degrees. Since we did not make BRDF measurements, these values were all set to one. The number of spectra, or curves, in each file was determined by the purpose of the dataset. Single and multiple coverage amounts were used in the DIRSIG simulation.

7.2.2   Asphalt

We will begin the discussion of our results with the measurements made on the asphalt. Two sets of measurements were made with each instrument: one in the reflective region and the other in the thermal. We will begin by addressing the effects that sand had on the reflectance of the asphalt in both regions and then we will move onto the effects of water on asphalt.

Figure **??** shows the results that we obtained using our asphalt and sand samples in the laboratory setting for coverage amounts ranging from 0 to 100%.

The ASD measurements demonstrate what was expected. The asphalt is very dark
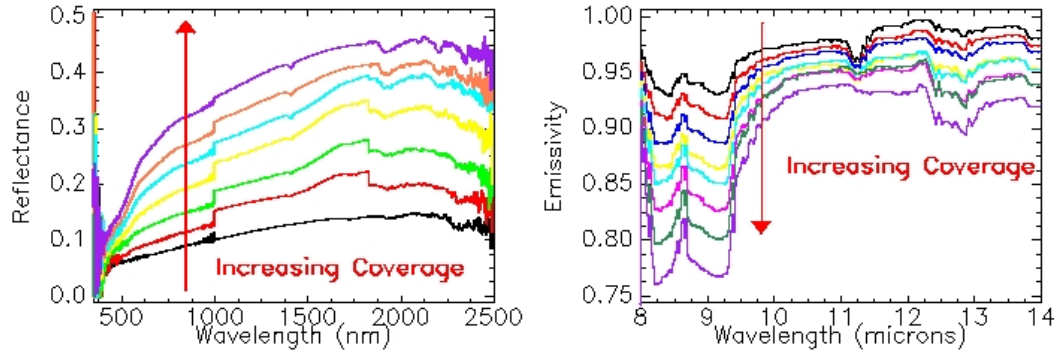
Figure 7.11: Asphalt & sand results: ASD (left) and D&P.

when compared to the sand and, therefore, the overall reflectance increases from that of the bare asphalt to the reflectance of the pure contaminant. While the reflectance changes, the overall shapes of the curves are also different. The asphalt spectrum is relatively flat, the sand is somewhat less so and contains features around 1.4 and 1.9 μm. These are water absorption bands and indicate that the sand did have some moisture content. This is not entirely unexpected as the sand samples were not dried thoroughly before each set of measurements were taken.

The problem with this dataset is that the discontinuities at 1000 and 1850 nm are still present. The rotating platform helped, but only marginally in this case. The results from other measurements indicate that this discontinuity should disappear or be much smaller than this current dataset shows. Further measurements would likely show this to be true.

The D&P results have a significant amount of features in comparison to the ASD results. There are a couple of features that are particular to quartz. The doublets between 8-9.5 μm and 12-13 μm are visible in this dataset. As previously mentioned, the sand that was used in these measurements was mad up primarily of silicates so we would

expect to see these features in increase as the amount of sand on the surface increases. The feature at 11.25 μm that disappears with increasing sand cover is a limestone feature. Since asphalt has a significant limestone content, this is not unexpected.

Once the results from the sand-asphalt combination had been analyzed, we continued our efforts with thin layers of water on the asphalt sample. As mentioned, there are few published results on the effect that thin layers of water can have on a substrate. The percentage coverage approach was not possible to duplicate for the water layers. Instead, we produced results that covered the range from zero to 100% coverage and interpolated values in between the two extremes.

Figure 7.12 contains the results of different water coverage amounts on the asphalt sample. Once again, the results of the upper- and lowermost curves represent the bare surface and pure contaminant states and the spectra in between do not necessarily represent the same coverage amounts.
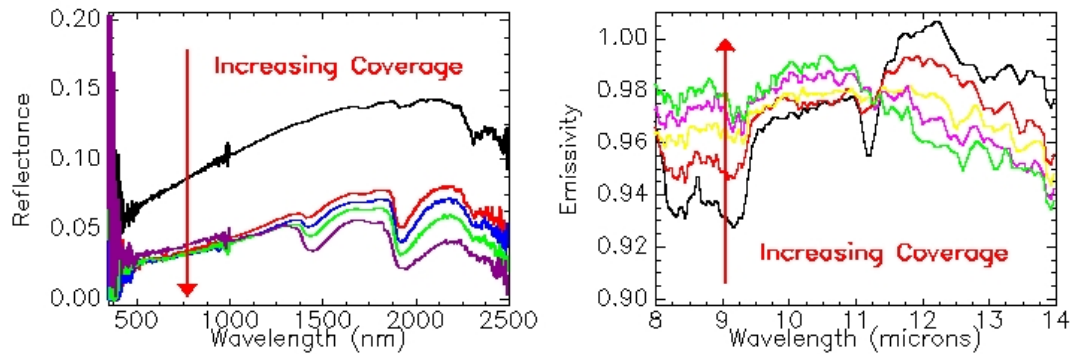

Figure 7.12: Asphalt & water results: ASD (left) and D&P.

The reflectance of the asphalt is reduced significantly over the reflective region. From our own experience, we know that wet asphalt is darker than dry asphalt and we would expect the spectra to show that. Indeed, it does not take very much water

on the asphalt surface for the reflectance to decrease by a large amount. The effect over the SWIR region is more complex but the results are somewhat intuitive as well. As we have already presented, the emissivity of a thick layer of water in the thermal region tends towards 1 or, conversely, the reflectance tends towards 0. As we pass from the VNIR to the SWIR region, we can see that the reflectance is further decreased. It is very likely that the saturation level of the asphalt sample was not high enough to push the reflectance of this sample to 0. Later on, when we look at the effect of water on concrete, it will be demonstrated that this tendency towards 0 is in fact true. For this case, however, it was very difficult to keep any significant amount of water on the surface. The main reason for this is that our asphalt sample was very porous and the water could pass through it like a sieve. With a better construction, a watertight sample box would allow for more water to stay on the surface.

The data over the LWIR, 8-14 μm, indicates the anticipated trend. As more water covers the surface of the asphalt, the emissivity tends towards 1. Once again, the maximum emissivity is not achieved in this case for the same reason mentioned in the previous section. Nonetheless, the trends are apparent. One interesting component in this region is the reversal of the spectra that occurs around 11 μm. Although the phenomenology surrounding this reversal is not fully understood, it is repeatable. Several approaches were taken to figure out the contributing factors to this feature, none of which were successful.

7.2.3   Concrete

The next material that we measured was the concrete sample. Since concrete is mostly sand, we did not expect that there would be significant differences between the reflectance of the contaminant and that of the surface itself.
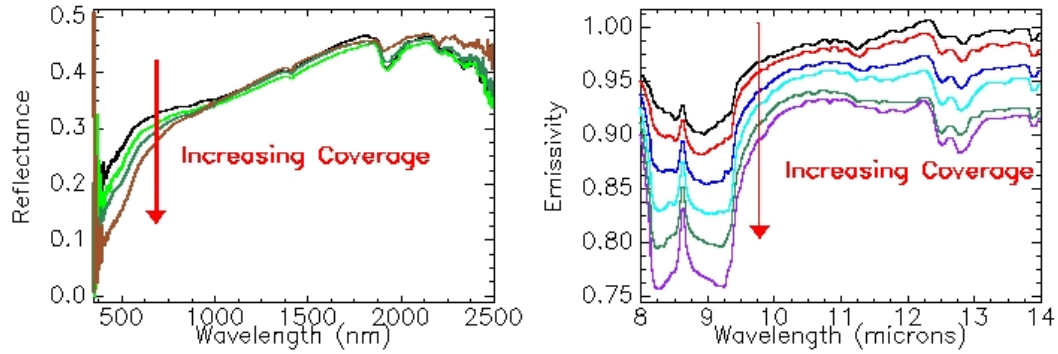
Figure 7.13: Concrete & sand results: ASD (left) and D&P.

Figure 7.13 shows that the sand has very little effect on the reflectance of the concrete. The sand that we used was, obviously, very similar to that used in the concrete sample composition. The changes that are significant over this region are in the VNIR region. Visually, the sand was darker than the concrete sample so one would expect the reflectance to decrease as the sand coverage increased.

The thermal region, however, did exhibit a change over the entire LWIR region as the sand coverage increased. The same features that increased in the asphalt set of measurements also increased here. The lowest reflectance is that of the pure contaminant and is the same as for the asphalt measurements. The initial curve for the concrete does show some of the same features as the pure contaminant. These features deepen as the coverage increases and the surface becomes more pure. The quartz features previously mentioned are expected to be in the bare concrete curve, but, since the sample does contain more than sand alone, they are lessened.

Adding water to most surfaces will make them darker. The degree to which the water decreases the reflectance is highly dependent on the initial reflectance of the bare, dry surface. With asphalt, the reflectance is quite low to begin with and therefore the

change with additional water will not be as significant as it could be for a brighter surface. For a comparison we will take a look at the results from the wet concrete measurements. Figure 7.14 shows the results of the ASD and D&P measurements.
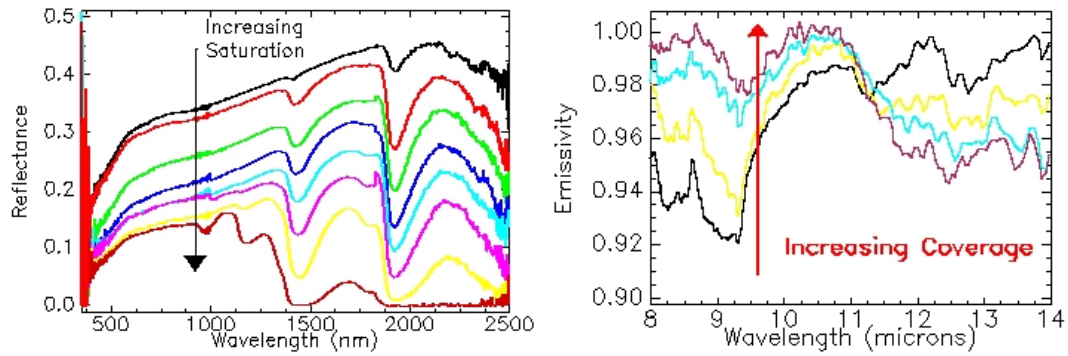

Figure 7.14: Concrete & water results: ASD (left) and D&P.

The ASD results clearly show that a reflectance of 0, or emissivity of 1, in the SWIR is attainable. More water was on this surface than the asphalt surface for the final measurement. The main reason for this is that concrete will allow water to be absorbed into the surface unlike the asphalt. As more water was added to the surface, the material itself retained increasingly more and more water. Water for the final measurement was pooled on top of the concrete and the layer of water was close to uniform over the instrument FOV. The water features at 1.4 and 1.95 μm deepen to the extent that the absorption is 100% and the reflectance is 0 at both of these wavelengths.

The data over the 8-14 μm range show the same trends for the concrete as seen with the asphalt. The emissivity increases towards 1 with increasing water on the surface. This trend reverses around 11 μm. The strong quartz features between 8 and 9.5 μm lessen with increasing water coverage.

7.2.4   Painted Metal

One of the more interesting surfaces that we measured was the red, painted metal. It was more interesting because the bare surface had a lot of features in it, more than the others. We did not make any measurements of the painted metal with water on it primarily because the ASD set-up required that the sample be rotated. A flat surface such as the painted metal would not retain any of the water once the potter's wheel began rotating. The results of the sand on the painted metal, however, could be measured by both instruments.
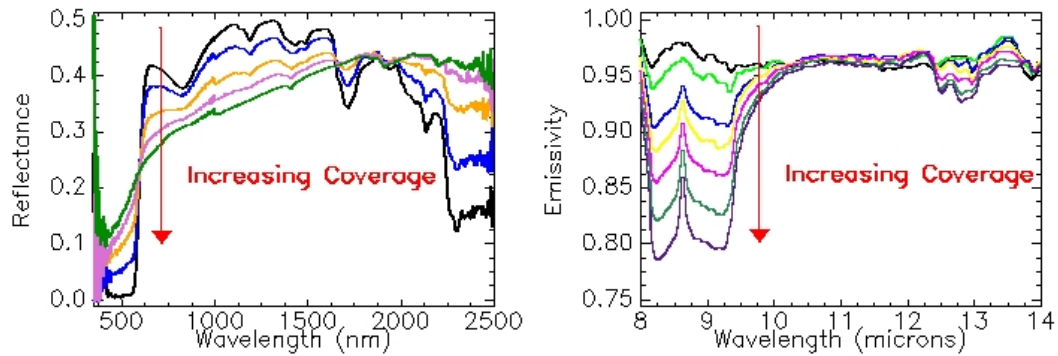

Figure 7.15: Painted metal & sand results: ASD (left) and D&P.

First, it is obvious is that the relationship of the reflectance as a function of percentage coverage, at different wavelengths, is not linear. The VIS region below 400 nm shows and increase in reflectance with increasing coverage, as expected, but then a reversal in the spectra occurs and from 600 to 1650 nm the reflectance decreases with increasing coverage. Another reversal happens at this point all the way to the end of the measurement range of the ASD. There is also a significant difference in the spectral characteristics of each of the materials. Sand is very spectrally smooth, no large features, over the entire reflective region. The painted metal, on the other hand, has

significant features throughout this region. The resulting curves show how the features flatten as the amount of sand coverage increases to 100%.

The D&P measurements follow the trend that was seen with the two previous materials. The quartz features between 8-9.5 μm and 12-13 μm are non-existent in the bare metal spectrum and deepen as the coverage is increased. The curves are very well-separated with increasing soil coverage.

7.2.5 Roofing Shingle

Although the discontinuities are significantly reduced in this dataset, the roofing shingle measurements do show small jumps in the spectra. Neither the sand nor the roofing shingle are very interesting. Both pure spectra are relatively featureless. The main change that occurs as the coverage increases is that the reflectance is increased up to that of the sand. The roofing shingle is spectrally flat across the VNIR/SWIR regions. The reflectance increases as the sand coverage is increased, with the greatest increase occurring over the SWIR region. The water absorption features, due to the moisture content in the sand, at 1.45 and 1.9 μm appear as before when the sand coverage increases.
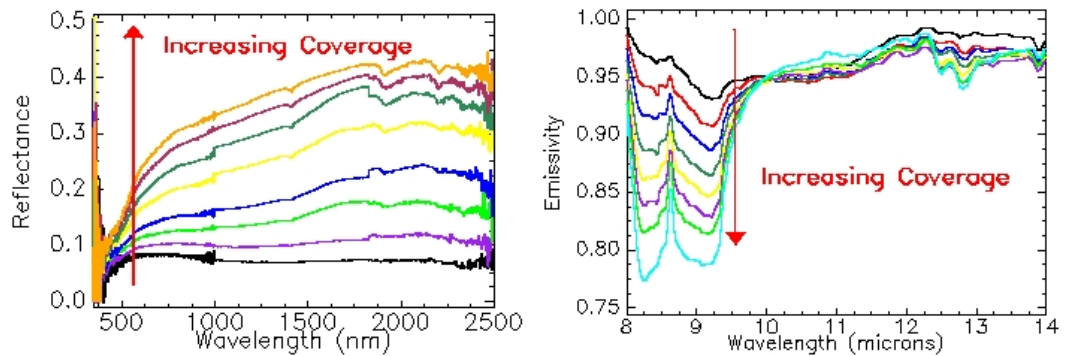

Figure 7.16: Roofing shingle & sand results: ASD (left) and D&P.

The D&P measurements are very similar to those previously seen. The initial measurement of the bare roofing shingle is relatively flat, although shallow quartz features are visible. These features deepen significantly with the coverage increase in sand coverage.

7.3   Error Estimates

In order to fully understand how close these values are to one another, an estimate of the error in each of the measurements must be made. The instruments have errors associated with them, as does the MISI image. The error for each of these was done in the traditional manner as shown in the following equation:

$$s_Y = [(\frac{\delta Y}{\delta X_1}s_{X_1})^2 + (\frac{\delta Y}{\delta X_2}s_{X_2})^2... + (\frac{\delta Y}{\delta X_N}s_{X_N})^2]^{1/2} \tag{7.1}$$

s_{X_i} is the error in the individual input variables. The partial derivatives of the dependent variable, Y, with respect to the input variables describe the sensitivity of Y to small changes in X [Schott (1997)]. Subsequent multiplication of the partial derivative by the error in the input variable generates the error in the Y. The square root of the sum of the squares is the total error. This is used because independent errors tend to add in quadrature.

The ASD and D&P can make very accurate measurements, however some error or uncertainty will always be present. The following two tables show the estimated errors in the reflectance measurements made by the ASD and the emissivity measurements made by the D&P. The values in these tables represent the best case scenario and the error could be much higher with a different scenario. For the D&P this is especially true. The measurements were made using the blackbody and changing the temper-

ature at which it was set. This allowed us to simulate a variety of temperatures for the downwelling and sample components of the governing emissivity equation already mentioned. The ASD measurements for these error calculations were made using tiles that were uniform, but not spectrally flat. Aside from these differences, both sets of measurements were made with the same instrument settings used in the material-contaminant combinations previously presented in this chapter. The errors stated in the following tables represent one standard deviation.

As Table 7.2 shows, the standard deviations change not only with wavelength but also with the reflectance of the tile for the ASD. The D&P error values also change as a function of the wavelength. Once these values were established, they were used to obtain the overall errors in the ratios presented earlier in this thesis. The error in the ratio also uses Equation 7.1. The final result is that the errors in the ASD reflectance values and the D&P emissivity values are very small. Errors for both instruments are significantly less than 1%. The errors in the ASD measurements also transfer to the error that may be assumed in the DIRSIG scene used in the modelling and validation.
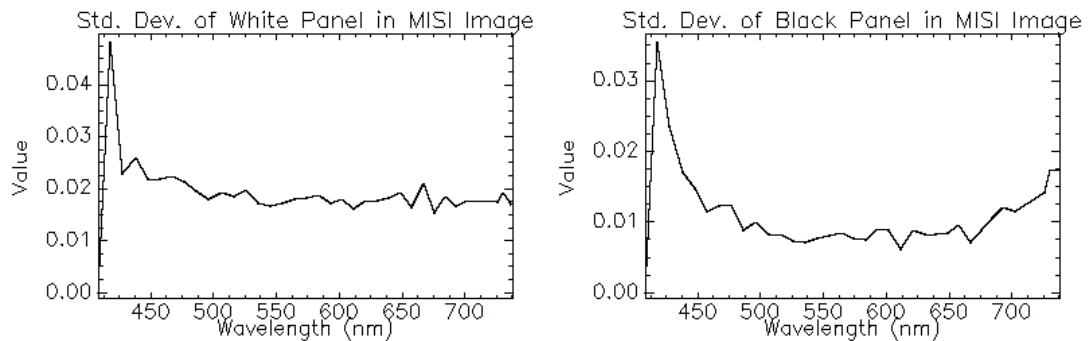

Figure 7.17: Error for MISI image: standard deviation values for the white and black calibration panels in the MISI image (reflectance)

Next, the error in the MISI image was characterized. As the plots of the MISI data show, the spectra are quite noisy. The error estimates were made using the calibration panels, both black and white, in the MISI image. The resulting values in the plots that follow indicate that the standard deviation changes as a function wavelength and with the different reflectance values between the panels.

Wavelength (nm)	Black tile error	Gray tile error
350	0.118965411	0.202980045
400	0.022944464	0.024500518
450	0.003555548	0.004360647
500	0.002532486	0.002604484
550	0.000892934	0.001311389
600	0.000995268	0.001090818
650	0.000941161	0.001059681
700	0.000727238	0.000824292
750	0.000657775	0.000867554
800	0.000618872	0.00068887
850	0.000788008	0.001076266
900	0.000883084	0.001379973
950	0.002071976	0.001613072
1000	0.003419299	0.004166567
1050	0.001058456	0.000943528
1100	0.000536619	0.000837752
1150	0.00067773	0.000661911
1200	0.000559849	0.000678134
1250	0.000551719	0.000622267
1300	0.00054612	0.000556474
1350	0.000415109	0.000590416
1400	0.000516409	0.000574289
1450	0.000391132	0.000536023
1500	0.000450911	0.000621536
1550	0.000467236	0.00066481
1600	0.000586902	0.000634824
1650	0.000543983	0.000652193
1700	0.000669363	0.000800788
1750	0.000668711	0.000859104
1800	0.000771153	0.00068634
1850	0.00247171	0.002183174
1900	0.002850765	0.002439908
1950	0.001881803	0.002155963
2000	0.002263794	0.002448192
2050	0.002865277	0.002804503
2100	0.003690709	0.002503512
2150	0.003831183	0.002735748
2200	0.004006161	0.00389721
2250	0.005218513	0.004760214
2300	0.005190056	0.005455696
2350	0.006586822	0.004879141
2400	0.010117395	0.011350647
2450	0.018431723	0.020603661
2500	0.087261016	0.055617243

Table 7.2: Error estimates for the ASD (reflectance)

Wavelength (microns)	Error in radiance for $T < T_{amb}$	error in radiance for $T > T_{amb}$
8.00026	0.076928115	0.153843965
8.50927	0.075640326	0.146358743
9.01084	0.072862118	0.138699734
9.51839	0.081542547	0.151577257
10.0235	0.074441872	0.141064959
10.5158	0.066180437	0.119989746
11.021	0.066435085	0.11484733
11.5356	0.07082348	0.126749129
12.01	0.071408998	0.129031033
12.5251	0.069519022	0.131612828
13.0332	0.061265462	0.114321131
13.5271	0.056970477	0.107354024
13.9986	0.055221981	0.104669242

Table 7.3: Error estimates for the D&P: errors for one standard deviation in the radiance values at temperatures less than and greater than the ambient temperature

Chapter 8

Model Development & Validation

8.1   DIRSIG Scene Generation

The next step after the data analysis was to come up with a way to use it within the structure of DIRSIG. As previously mentioned, DIRSIG will allow us to create synthetic scenes based on digital images. For our work, we used an image of the RIT campus taken by MISI, to validate our results. Before we could do this, however, we chose the material-contaminant combinations that would work within our scene. Given that the model of the campus that we used contained many parking areas, we chose asphalt as the material and both contaminants, sand and water. Within the scene, there was also an area that was close to a construction area. Leading to and from this area were trails of sand on top of the asphalt parking lot. This was an ideal spot for validation of soil coverage of asphalt. The image below shows the area of the scene that we used in our modelling efforts.

The highlighted areas indicate the water spot (upper left of Figure 8.1) that was used in the validation of the asphalt-water combination and the area on the bottom

Figure 8.1: MISI image of campus scene collected on 21 October 2005

right shows the subset used for the DIRSIG scene. The subset contains the sand trails from the construction site. In the upper-right of the original image there are two areas, one black and the other white. These two areas are approximately 100' by 100' and are painted areas used for the empirical line method (ELM) atmospheric compensation of each image. Using the ELM allowed us to convert the MISI image digital count values and the DIRSIG radiance values, respectively, into reflectance. This was necessary because the VNIR bands in MISI are not radiometrically corrected. The ground truth reflectance measurements of the panels were made with the ASD.

The next step in this process was to define the different materials within the scene.

Since we were only interested in the asphalt areas, many of the other classes were not well-defined, i.e. grass or vehicles. The material map in Figure 8.2 identifies three main classes: grass (white), asphalt (dark grey) and contaminant areas (dark greys). We will ignore the light grey area for now since it is simply a placeholder for a building. The MISI image of the same area is included for comparison.
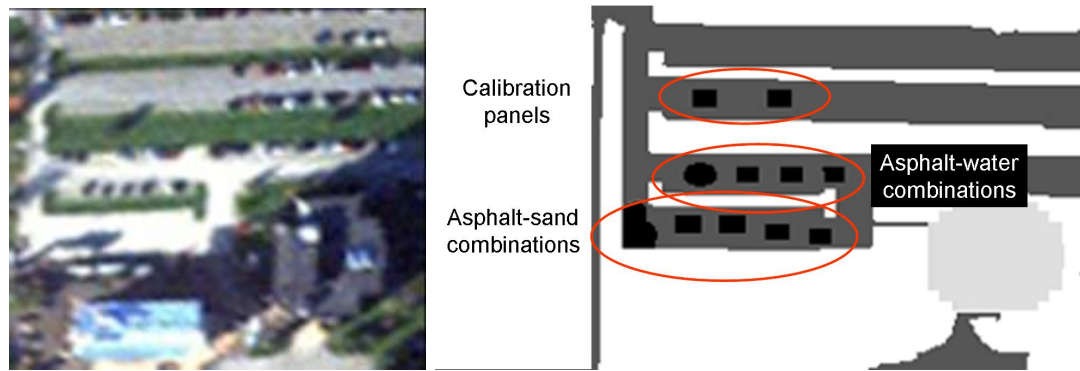

Figure 8.2: Material map for DIRSIG scene: MISI image (left) and material map (right)

The contaminant areas on the material map are placeholders for the asphalt and contaminant combinations. In Figure 8.2, the placeholders on the second asphalt row are for the black (left) and white (right) calibration targets, the third row contains the asphalt-water combinations and the fourth row has the asphalt-sand combinations. While these areas may appear as though they are black, closer inspection would reveal that they in fact each have slightly different material identification numbers (IDs), as do all of the other regions. These material IDs allow for a link between the material image and the emissivity files. Therefore, each contaminant area draws its reflectance values from a specific emissivity file. The resulting format of the emissivity files used by DIRSIG are in Appendix C. Table 8.1 lists the various coverage combinations as they are shown in the image, from left to right, on each row. The coverage amounts

were calculated using the functional relationships determined by the IDL program in Appendix B. These relationships allowed us to calculate any coverage amount between 0 and 100%.

Material, contaminant	% coverage	% increment	# of curves in *.ems file
Asphalt, water	0 to 100	2	51
	20	-	1
	50	-	1
	70	-	1
Asphalt, sand	0 to 100	1	101
	20	-	1
	40	-	1
	60	-	1
	80	-	1

Table 8.1: Dataset used for implementation into DIRSIG

From the skeleton material image, a DIRSIG scene was created by applying the MISI scene model and using the same parameters as defined for the real data collection. The wavelength range of MISI covers the visible, near-infrared and thermal regions, however our analysis will be restricted to the visible and near-infrared regions. It is much easier to see in this image how the contaminant levels change in each of the different areas. The sand spots become brighter and the water spots become darker as the coverage increases. This is the scene from which all of the following validation plots have been taken for analysis.

8.2   Validation

The final step in this research was to validate the DIRSIG image with the truth data from MISI. We tackled this by assessing the different material-contaminant areas in the DIRSIG scene and comparing the results with similar regions in the MISI image.

Figure 8.3: DIRSIG scene with contaminants

In all cases, the comparisons are made between atmospherically compensated surface reflectance spectra from MISI and DIRSIG. First we will review the measurements for asphalt and sand, then the asphalt and water areas.

8.2.1   Asphalt & Sand Validation

There were five different asphalt and sand combination areas in the DIRSIG image. Four areas represented 20, 40, 60 and 80 percent coverage, respectively, and the fifth area was a simulation of a variety of coverage amounts. This final area will be compared against sand trails that may be found in the MISI image.

Since each of the pure coverage amount areas were simulated with the real data from the laboratory measurements, it is only reasonable to assume that both sets will conform. The proof is shown in Figure 8.4, with each successive measurement in a different colour, and it demonstrates how well the datasets align.

The results overlap so accurately that putting all of them on one plot results in the inability to tell the two datasets apart.
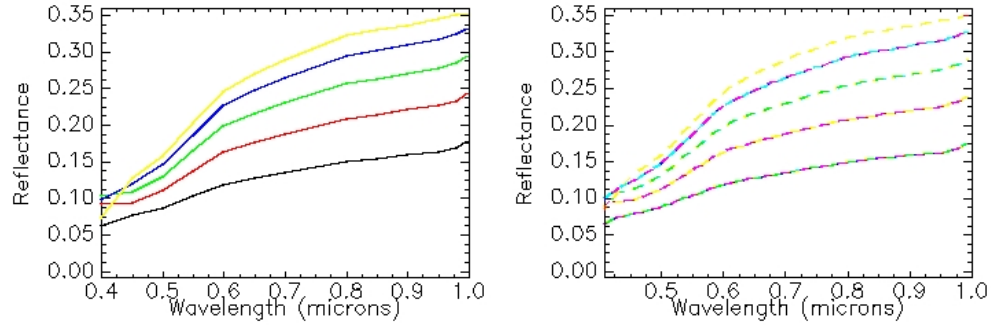
Figure 8.4: Validation of laboratory measurements (left) vs. DIRSIG for sand on asphalt: coverage %: 20 (black), 40 (red), 60 (green), 80 (blue), 100 (yellow)

The results shown above are what one would expect. For the sand tracks on the asphalt, the coverage is not 100% and several different percentage coverage amounts may be represented in a small area, even over one pixel. Using ENVI once again, we selected an area that was 3x3 pixels in size and compared the results obtained from the MISI image to those found in the DIRSIG scene.
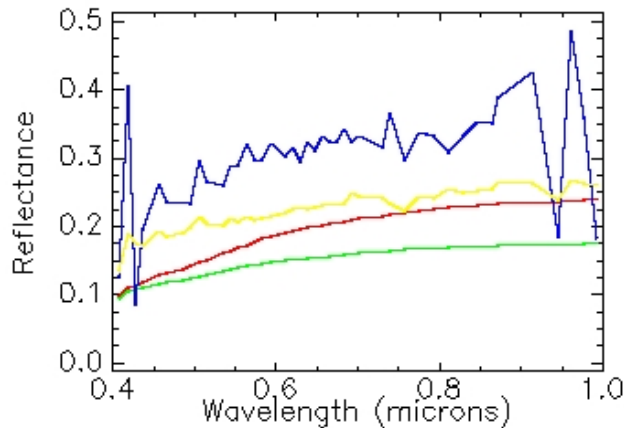

Figure 8.5: Comparison of bare and sand covered asphalt in MISI (bare asphalt: yellow, sand covered asphalt: blue) and DIRSIG (bare asphalt: green, sand covered asphalt: red)

Figure 8.5 contains four curves: two for each of MISI and DIRSIG. The blue and yellow spectra represent the MISI reflectance values for sand covered and bare asphalt, respectively. The same is true of the red and green spectra for DIRSIG. Despite using an average of a 3x3 pixel region of interest, the MISI image is still quite noisy. At first glance, one would think that these results indicate that MISI results yield different reflectance values than those found in DIRSIG, or taken in the laboratory setting. Clearly, the magnitude of the two sets of curves is quite different. However, if we take the ratio of each set of curves, dividing the sand covered values by their bare asphalt counterparts, the differences are not as great.

The purple curve in Figure 8.6 is the result of this ratio from the MISI image and the green curve is the ratio from the DIRSIG scene. These results show that, regardless of the manner in which the data was acquired, the ratio of the two curves remains very close to the same. This is a great result given that the soil and asphalt samples used in the laboratory were not the same as those found in the MISI scene. In fact, the asphalt and sand were both significantly darker, newer asphalt and a different mixture of sand, in the laboratory than in the real scene. This information could be quite useful in the analysis of images and the impact on target reflectance or scene statistics could yield interesting results.

8.2.2 Asphalt & Water Validation

The last set of comparisons to be made are for different amounts of water on asphalt. The same approach was taken for these comparisons as was done in the previous section. The main difference between the validation of water on asphalt versus sand on asphalt is that water is not opaque over this region. This means that the difference in the background material reflectance is likely to have a significant impact on the results. As
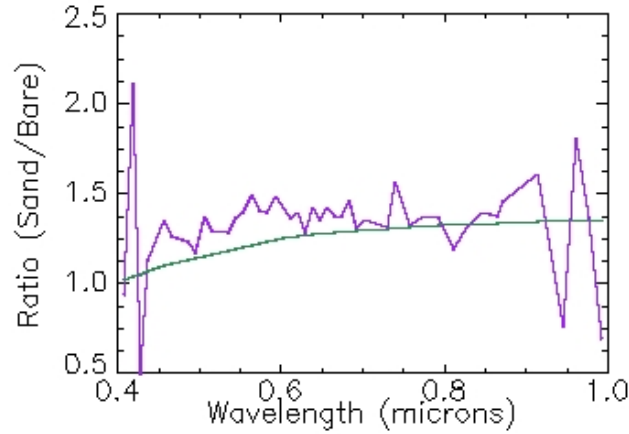
Figure 8.6: Ratio of sand on asphalt to bare asphalt in MISI and DIRSIG

before, we will begin by comparing the laboratory results to those incorporated into DIRSIG.

Figure 8.7 shows that most of the curves are in line and match reasonably well to each other. All curves except that of the bare asphalt (blue curve). The reason for this is simple: we are not dealing with the same starting point. The lab sample of asphalt was significantly darker than the one in the DIRSIG scene which is modelled after the original MISI scene. Our lab sample was cleaned before each set of measurements and it was very difficult to find asphalt pixels within the DIRSIG scene that were as clean as our laboratory sample.

The way that DIRSIG assigns a reflectance value to each pixel is determined by the class that it belongs to. As you can see by the material map, all areas outside of the contaminant spaces are one class and correspond to one emissivity file with many curves. In this case the emissivity file for asphalt contained sand coverage amounts from 0 to 100 % . There are also small differences between the laboratory values and those in DIRSIG for the other coverages but they are all within an acceptable limit
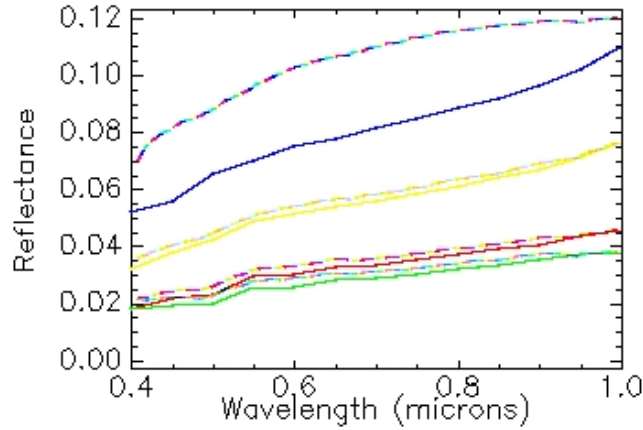
Figure 8.7: Validation of laboratory measurements (solid) vs. DIRSIG for water coverage of asphalt: Coverage amount in %: 0 (blue), 20 (yellow), 50 (red), 70 (green)

$(\rho < 0.005)$.

Figure 8.8 shows the same set of four curves, one set for each of MISI and DIRSIG. The yellow and blue curves are from the MISI image and represent the bare asphalt and water covered asphalt. The same is true for the green and red curves from the MISI scene, respectively. As with the sand spectra, the magnitude of each of these curves is significantly different. By taking the ratio as we did before, we can see if the two sets of measurements are similar within their own scenes.

Dividing the contaminant spectrum by the bare surface spectrum as before, for each MISI and DIRSIG, yields a ratio of the wet to dry asphalt curves. As shown in Figure 8.9, the ratio curves are remarkably similar. By dividing through in the same manner as for the sand curves, we can see how the ratio changes with these two different contaminants. Since the sand increased the reflectance of the asphalt, the ratio was greater than 1. The reverse for the darkening effect of the water on the asphalt is also true and the ratio is less than 1.
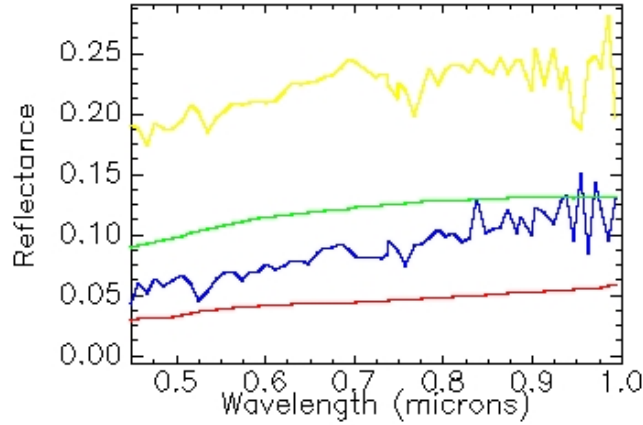
Figure 8.8: Comparison of bare and water covered asphalt in MISI (bare asphalt: yellow, water covered asphalt: blue) and DIRSIG (bare asphalt: green, water covered asphalt: red)

These modelling results indicate that it is possible to understand the trends among spectra in one environment and transfer that knowledge to another. The quantitative approach to the laboratory measurements gave us a strong understanding of how sand and water alter the reflectance spectra of asphalt and the remaining three materials. Taking the next step to incorporate these measurements into a DIRSIG scene allowed us to make comparisons with the real world imagery taken by MISI. These two scenes offered the ability to validate the data from a controlled laboratory setting to that of a remotely sensed imagery with significantly less control placed on it.
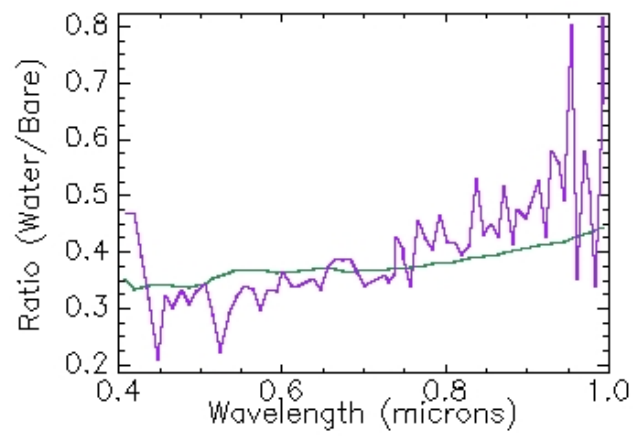
Figure 8.9: Ratio of water on asphalt to bare asphalt in MISI and DIRSIG

Chapter 9

Conclusion

The objectives of incorporating selected environmental effects into DIRSIG were accomplished. Although the manner in which this was done does not yet allow the user to define how much soil or water they would like on a specific surface, the ground work has been laid.

The qualitative measurements made in the field helped to validate the anticipated trends and results before making measurements in the laboratory. These results provided some initial measurements for future work. Once we moved into the lab, we continued with the validation of previously published results and we also set out to make our own contributions.

Three main areas were original contributions from the measurements in the laboratory. The first of these was the instrument set-ups used for both the ASD and the D&P in the laboratory. The rotating platform for the ASD improved the quality of the measured spectra and allowed to make measurements of surfaces that would have ordinarily been very difficult to process. The D&P ice tray set-up also made it possible to use an emissive field instrument in the laboratory with a high degree of success.

The second contribution was made by making coverage measurements of sand on a variety of background materials. To the best of our knowledge the measurements that have been made up to this point by other researchers have concentrated on full FOV coverage of varying depths. Finally, thin layers of water have not been measured to any degree of depth by the remote sensing community. Water posed some interesting questions insofar as its interaction with substrates and the effect that it would have in the overall spectral reflectance.

The results of these measurements demonstrated that material-contaminant combinations were highly linear with increasing coverage over the emissive thermal region and that second order polynomial fits were required for the reflective region. Using the knowledge of the percentage coverage for each measurement made, these relationships were determined and then used to create specific coverage amounts for use in the DIRSIG emissivity files.

The laboratory results were validated against a MISI image. Although only one material, asphalt, with both the water and sand contaminants was incorporated into the DIRSIG scene, we were able to obtain some interesting and satisfying results. The modelling efforts were validated with the real data by calculating the ratio of a bare asphalt region with a contaminated region for each contaminant in both the modelled and real scenes, respectively. The final results show that we were able to create a modelled scene with laboratory measurements that was very similar to real measurements made with our airborne sensor when comparing the ratio of similar regions in each scene.

Chapter 10

Future Work

Research in any area usually raises more questions than it answers. This work is no different. There are several areas for improvement or extension that should be mentioned at this point.

It would be interesting to compare apples with apples for scene generation and validation. The example that comes to mind is the laboratory asphalt sample that was different from the asphalt in the MISI scene. While this did not hurt our results, it would be interesting from a validation perspective to make a comparison of the magnitude. Along the same line, the other materials that were measured in the lab should also be incorporated into a DIRSIG scene. The extension of this would be to measure many other materials to be included into a scene as well.

The validation of our data was only done in the VNIR region but DIRSIG has the capability to simulate imagery at longer wavelengths. The question still remains as to how the full spectrum modelling would be accomplished. This cannot be done without the MWIR measurements that are missing from the current dataset. Hopefully, it will be possible to include these measurements in an additional dataset.

A more mathematically rigorous approach to this modelling may also lead to a way in which the background spectrum can be pulled from a contaminated pixel spectrum. This information would be useful when attempting to unmix pixels. Although it appears at this stage that the contaminated spectrum is highly dependent on the underlying material, this would require further analysis and measurements to determine. It would also be interesting to investigate the change in target detection performance using a matched filter for a target in a pristine background versus one in a contaminated background.

User controlled parameters within DIRSIG would allow anyone to create a scene with sand or water contamination without having to use precomputed emissivity files for a limited number of materials.

The instrument set-up was very effective but does require some refinement. The D&P set-up especially took up a significant amount of room and could be improved by using better materials. The ice kept the "sky" quite cold, but it required new ice each day. A more permanent or recycling cooling method would be more effective. The ASD illumination sources were sufficient but could also be made better by using higher wattage light sources and a better power source. Both set-ups should be further validated with additional measurements.

Further investigation and research into the reversal trend that we saw with increasing water coverage should be done. Focus on this area in particular may help to reveal the cause or phenomenology behind this trend.

Appendix A

Percentage coverage calculations

The following figures and table illustrate the steps involved in calculating the image statistics and percentage coverage of sand on each of the materials.

For each contaminant, a digital image was taken of the contaminant on the material being measured. This image typically contained a ruler placed on the surface so that it was possible to truncate the image down to the FOV of the instrument. The approximate size of the FOV was known from the manufacturer's specifications for each instrument. The first image shown is an example of three optically thick piles of sand on the painted metal.

Figure A.1: Sand on painted metal (original image)

Using our knowledge of the FOV size, the original image could be truncated from a rectangular image to the round FOV. The FOV of the instrument was cut out of the original image and pasted into a new environment that would allow us to separate the area outside of the FOV. The sand areas were blended somewhat to allow for a more uniform appearance. This was necessary in order to effectively threshold the image.

The sand had many different constituents, some dark and others light in colour. Since the thresholding was done based on the digital count values of each pixel, the sand area had too many different values. The blending simply kept the sand pixels closer to the same digital count value. The image on the left of A.2 is the thresholded image.

ENVI has several different classification methods that allow an image to be separated into different areas that are similar in content. In this case, our image had very distinct regions based on the thresholding (black for the material and white for the contaminant) and the image background (yellow). The yellow area does not contain any information about the material or contaminant and is simply the background of the image needed to fill out from the round FOV to the square image.

The simplest classifiers use an unsupervised method in which the user selects a few stop parameters and allows the computer to process the image. For more complicated scenes this is not always effective. However, since our scene was quite simple, kmeans classification, an unsupervised method, proved quite accurate. The number of classes was set at five. The image on the right of A.2 is the classified image.
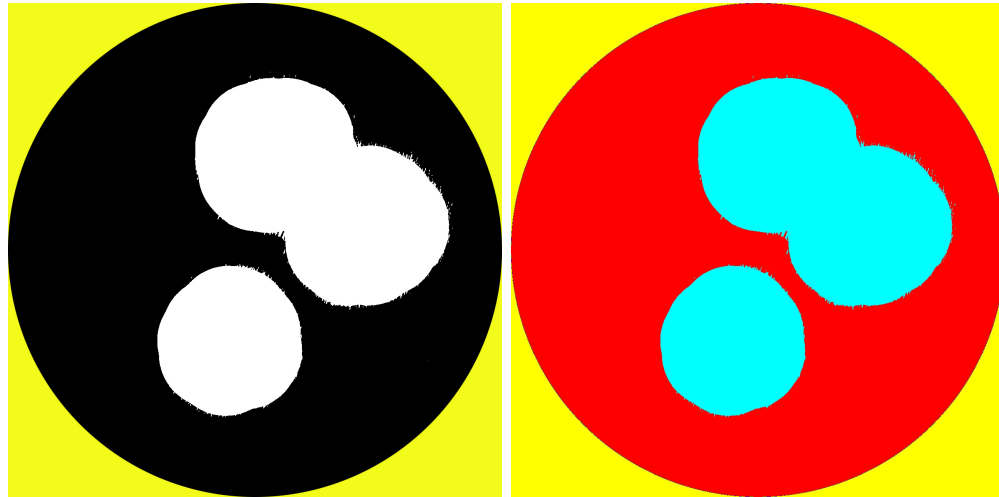

Figure A.2: Sand on painted metal (thresholded image on left) and classified image

Using the post classification statistics report in ENVI, we could then obtain the number of pixels for each class and calculate the percentage coverage. Outside the FOV of the instrument, there is a class of pixels (yellow). This is not actually part of the original image nor is it representative of anything within the FOV.

From Table A.1, the percentage coverage is:

$$\frac{396726}{396726 + 808365} * 100 = 32.9\%$$

Class Distribution Summary
Unclassified:	0 points
Class 1:	808,365 points
Class 2:	1,615 points
Class 3:	1,503 points
Class 4:	1,793 points
Class 5:	396,724 points

Table A.1: ENVI statistics report
Class - colour: 1 - red, 2 - green, 3 - blue, 4 - yellow, 5 - cyan

Classes 2, 3 and 4 represent pixels at each of the transitions and do not drastically change the percentage of coverage. They have been excluded in this example.

The percentage coverage values for each set of measurements was needed to calculate the relationship between the reflectance and percentage coverage at discrete wavelengths. This information was used in the IDL program in Appendix B for the modelling of each contaminant-material combination.

Appendix B

IDL program

The following is the IDL program that was written to calculate the relationship (quadratic, in this case) between the reflectance and the percentage coverage of soil on a surface. Once calculated, these relationships were used to generate new curves at selected percentage coverage values. This allowed us to compare different datasets with the same coverage amounts. The output of this program is a text file that was used to generate the emissivity (*.ems) files for DIRSIG use.

```
pro cov_asph

;main file with coverage and emissivity values
ff = pickfile()

;file with wavelength values
rr = pickfile()
data = read_ascii(ff)
data = data.(0)
result=dblarr(44,3)

;find the coefficients of a second order polynomial that fit each of the datasets, at
discrete wavelength intervals detailed in the files above
for i = 1L, 44 do begin
    result[i-1L,*] = poly_fit( reform(data[0,*]),
    reform(data[i,*]),2, /double )
endfor
print,'Asphalt Coefficients:'
print, result
```

```
f=dblarr(44,11)

;equations for each dataset using the coefficients
for i=1,44 do begin
    for j=0,10 do begin
```
$$f(i-1,j) = result[i-1,0] + result[i-1,1]*data[0,j] + result[i-1,2]*(data[0,j])^2$$
```
    endfor
endfor

asph1=read_ascii(rr)
asph1=asph1.(0)

;array of wavelengths
asphwave=asph1[0,*]

;plots of calculated data
window, 1
plot, asphwave, asph1[1,*], xr=[350,2500], xstyle=1
for i=0,10 do begin
    oplot, asphwave, f[*,i], co=3e8
endfor

;plots of measured data
for i=1,11 do begin
    oplot, asphwave, asph1[i,*], co=255
endfor

;error calculation - difference between measured and calculated values
sub = reform(asph1[1,*]) - f[*,0]
sub1 = reform(asph1[2,*]) - f[*,1]
sub2 = reform(asph1[3,*]) - f[*,2]
sub3 = reform(asph1[4,*]) - f[*,3]
sub4 = reform(asph1[5,*]) - f[*,4]
sub5 = reform(asph1[6,*]) - f[*,5]
sub6 = reform(asph1[7,*]) - f[*,6]
sub7 = reform(asph1[8,*]) - f[*,7]
sub8 = reform(asph1[9,*]) - f[*,8]
sub9 = reform(asph1[10,*]) - f[*,9]
sub10 = reform(asph1[11,*]) - f[*,10]
```

```
window,2
plot, asphwave, sub, xrange=[350,2500], xstyle=1, yrange=[-0.1,0.1], ystyle=1
oplot, asphwave, sub1, co=255
oplot, asphwave, sub2, co=3e8
oplot, asphwave, sub3, co=2e9
oplot, asphwave, sub4, co=1e7
oplot, asphwave, sub5, co=4e7
oplot, asphwave, sub6, co=4e8
oplot, asphwave, sub7, co=5e4
oplot, asphwave, sub8, co=9e9
oplot, asphwave, sub9, co=4e8
oplot, asphwave, sub10, co=5e4

;calculate emissivity values using coefficients
;coverages from 0 to 100 %
y=dblarr(44,101)
cover=indgen(101)

for i=1L,44 do begin
    for j=0,100 do begin
```
$$y(i-1,j) = result[i-1,0] + result[i-1,1] * cover[j] + result[i-1,2] * (cover[j])^2$$
```
    endfor
endfor

;output file with all of the reflectance values for the above coverage percentages
```
$status = \mathrm{WRITE\_SYLK}('C : \backslash asph\_0to100.slk', y)$
```
;plot of all spectra from 350 to 2500 nm, for 0 to 100% coverage

window,3
plot, asphwave, y[*,0], xr=[350,2500], xstyle=1

;modelled coverages
for j=0,100 do begin
    oplot, asphwave, y[*,j], co=3e8
endfor
end
```

Appendix C

Emissivity file format

An emissivity database file (EMS) contains a set of diffuse emissivity curves for a given material. This file also contains an angular weighting function to compute the specular emissivity for a given zenith angle (from the vertical) [`http://dirsig.cis.rit.edu`].

10		The number of curves in the file
1.00		Normal spectral emissivity weighting factor for 0° off normal
1.00		Normal spectral emissivity weighting factor for 1° off normal
...		
1.00		Normal spectral emissivity weighting factor for 90° off normal
CURVE_BEGIN		Marks the start of a new curve
0.400	0.6865	Wavelength [microns] and emissivity pair
0.410	0.6654	Wavelength [microns] and emissivity pair
...		
14.490	0.9102	Wavelength [microns] and emissivity pair
14.500	0.9187	Wavelength [microns] and emissivity pair
CURVE_BEGIN		Marks the start of a new curve
0.400	0.6845	Wavelength [microns] and emissivity pair
...		
14.500	0.9197	Wavelength [microns] and emissivity pair
$End-of-file$		

Table C.1: Sample emissivity file for DIRSIG (with comments)

Appendix D

Vehicle Measurements

The following images and plots represent the qualitative measurements that were made on the vehicle listed in the Table 7.1. The Subaru, Focus and Saturn measurements were chosen specifically to indicate how different the spectra can be between different vehicle types and colours. In the analysis of these results, the common trends were also apparent.
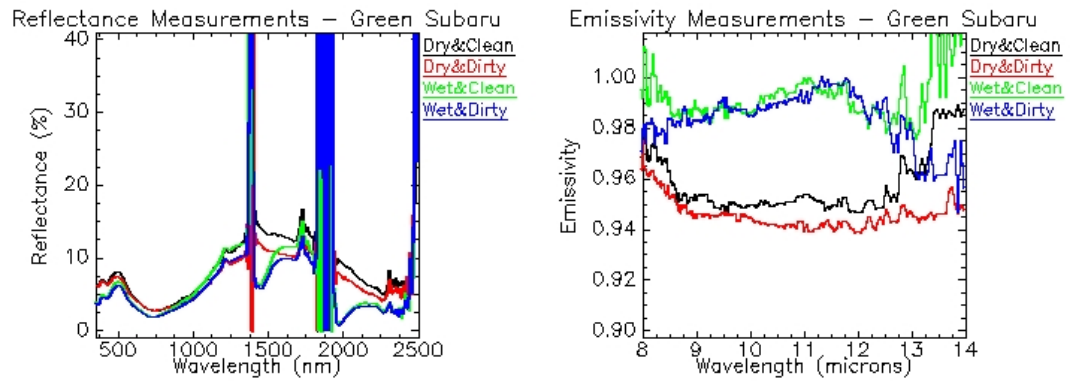
Figure D.1: Subaru set-up

Figure D.2: Subaru ASD (left) and D&P measurements: dry & clean - black, dry & dirty - red, wet & clean - green, wet & dirty - blue

Figure D.3: Focus set-up
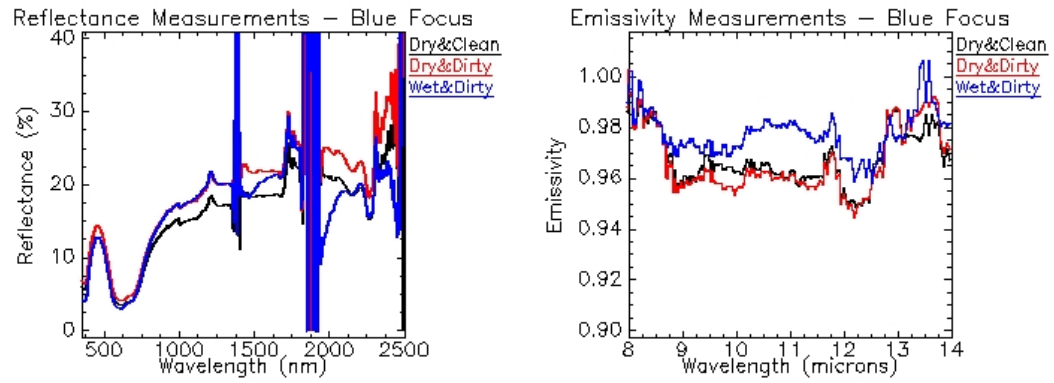
Figure D.4: Focus ASD (left) and D&P measurements: dry & clean - black, dry & dirty - red, wet & dirty - blue. Note that no data could be processed for the wet & clean surface condition and therefore no spectrum is plotted for this combination.
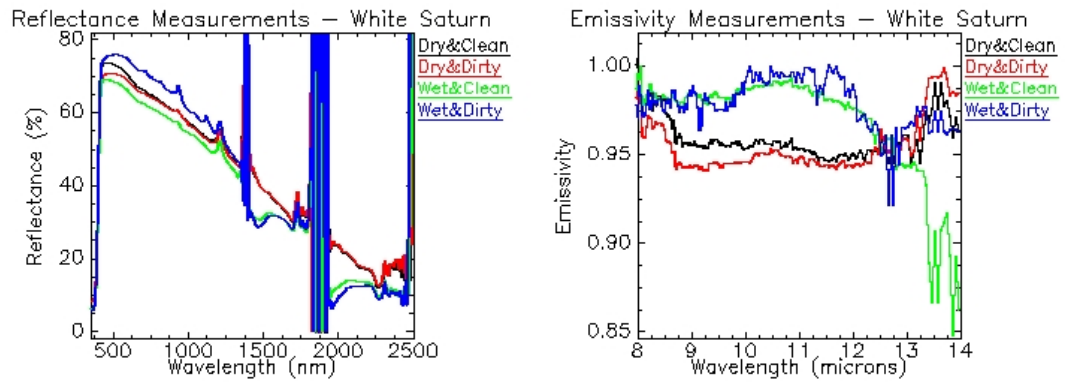
Figure D.5: Saturn set-up

Figure D.6: Saturn ASD (left) and D&P measurements: dry & clean - black, dry & dirty - red, wet & clean - green, wet & dirty - blue

Appendix E

Functional Relationships

The following plots show all of the measurements made in the laboratory. These plots show the functional relationships that exist between each of the material-contaminant combinations as the coverage is varied between 0 and 100%.
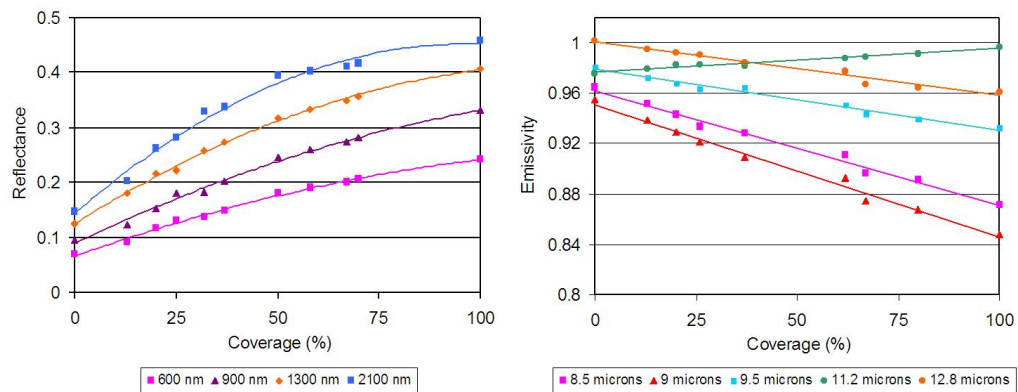

Figure E.1: Asphalt and sand: non-linear over the reflective region (left) and linear over the emissive region
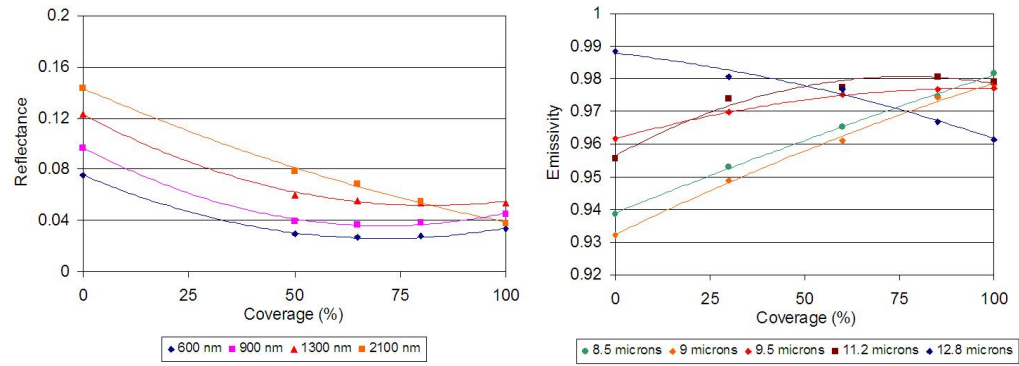
Figure E.2: Asphalt and water: non-linear over the reflective (left) and emissive regions
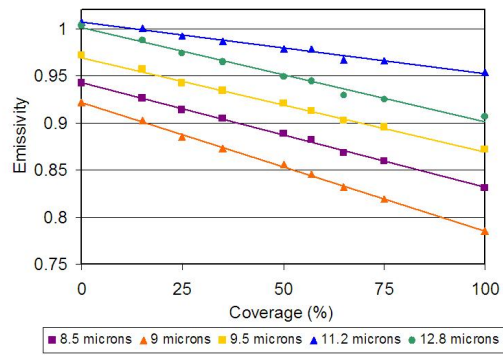

Figure E.3: Concrete and sand: linear over the emissive region. The reflective region is not shown since the spectrum over this region does not change with increasing sand coverage.
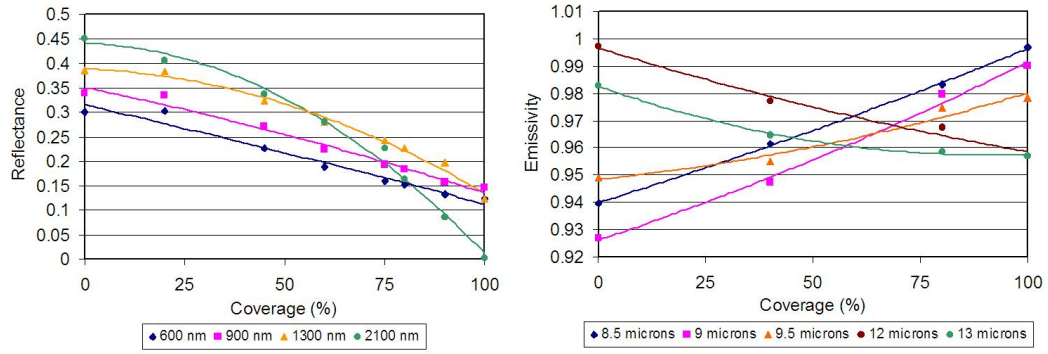
Figure E.4: Concrete and water: non-linear over the reflective (left) and emissive regions
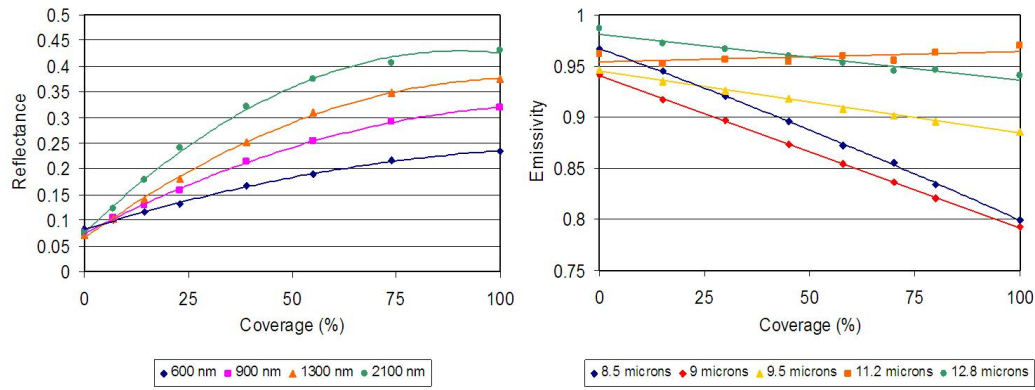

Figure E.5: Roofing material and sand: non-linear over the reflective (left) and linear over the emissive regions
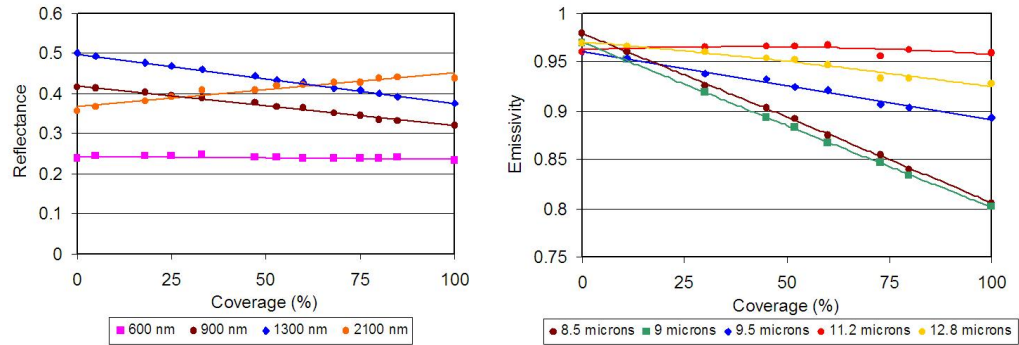

Figure E.6: Painted metal and sand: linear over the reflective (left) and emissive regions

Bibliography

`http://www.asdi.com`. Information for Analytical Spectral Devices (ASD) FieldSpec Pro Spectroradiometer.

http://www.asphaltinstitute.org/.

`http://www.dirsig.org`.

`http://www.labsphere.com`.

M. Baumgardner. *Resource Inventory and Baseline Study Methods for Developing Countries*, volume 83. Amer. Assoc. Adv. Sci., 1985.

M. F. Baumgardner, L. F. Silva, L. L. Biehl, and E. R. Stoner. Reflectance properties of soils. *Advances in Agronomy*, 38:1–44, 1985.

S. Bowers and R. Hanks. *Reflectance of radiant energy from soils*, volume 100. Soil Sci., 1965.

Carl Salvaggio. Infrared field spectra collection protocol. November 2000.

R. N. Clark. *Remote Sensing for the Earth Sciences: Manual of Remote Sensing*, volume 3, chapter 1. John Wiley and Sons, New York, 1999.

DIRS Lab. Analytical spectral devices sequence of events. `www.cis.rit.edu`, March 2004.

DIRS Lab. Visible, near infrared, and short wave infrared spectra collection protocol. `www.cis.rit.edu`, July 2003.

D&P Instruments. *Model 102 Portable FTIR Instruction Manual*. May 2004.

B. Hapke. *Theory of Reflectance and Emittance Spectroscopy*. Cambridge University Press, 1993.

B. Hapke. Bidirectional reflectance spectroscopy: 5. the coherent backscatter opposition effect and anisotropic scattering. *Icarus*, 66:523–534, 2002.

G. Hunt and J. Salisbury. volume 2. Mod. Geol., 1971.

G. Hunt and J. Salisbury. volume 5. Mod. Geol, 1976a.

G. Hunt and J. Salisbury. volume 5. Mod. Geol., 1976b.

IOCCG (2000). Remote sensing of ocean colour in coastal, and other optically-complex, waters. In S. Sathyendranath, editor, *Reports of the International Ocean-Colour Coordinating Group*, number 3, Dartmouth, Canada. IOCCG.

J. R. Johnson, P. G. Lucey, K. A. Horton, and E. M. Winter. Infrared measurements of pristine and disturbed soils: 1. spectral contrast differences between field and laboratory data. *Remote Sensing of Environment*, 64:34–46, 1998.

D. B. Lobell and G. P. Asner. Moisture effects on soil reflectance. *Soil Sci. Soc. Am. J.*, 66:722–727, 2002.

H. J. Mitchell and C. Salvaggio. Methodologies and protocols for the collection of mid-wave and longwave infrared emissivity spectra using a portable field spectrometer. In *Proceedings of SPIE – Volume 4381, Algorithms and Technologies for Multispectral, Hyperspectral, and Ultraspectral Imagery VII,*, pages 539–548. SPIE, 2001.

H. J. Mitchell and C. Salvaggio. MWIR and LWIR spectral signatures of water and associated materials. In S. S. Shen and P. E. Lewis, editors, *Proceedings of SPIE – Volume 5093, Algorithms and Technologies for Multispectral, Hyperspectral, and Ultraspectral Imagery IX*, pages 195–205. SPIE, 2003.

J. E. Moersch and P. R. Christensen. Thermal emission from particulate surfaces: A comparison of scattering models with measured spectra. *Journal of Geophysical Research*, 100(E4):7465–7477, April 1995.

J. F. Mustard and J. E. Hays. Effects of hyperfine particles on reflectance spectra from 0.3 to 25 μm. *Icarus*, 125:145–163, 1997.

G. S. Okin and T. H. Painter. Effect of grain size on remotely sensed spectral reflectance of sandy desert surfaces. *Remote Sensing of Environment*, 89:272–280, 2004.

T. H. Painter, J. Dozier, D. A. Roberts, R. E. Davis, and R. O. Green. Retrieval of subpixel snow-covered area and grain size from imaging spectrometer data. *Remote Sensing of Environment*, 85:64–77, 2003.

R. M. Pope and E. S. Fry. Absorption spectrum (380-700 nm) of pure water. II. integrating cavity measurements. *Appl. Opt.*, 36:8710–8723, 1997.

J. W. Salisbury and D. M. D'Aria. Emissivity of terrestrial materials in the 8-14 μm atmospheric window. *Remote Sens. of Environ.*, 42:83–106, 1992.

J. W. Salisbury and D. M. D'Aria. Emissivity of terrestrial materials in the 3-5 μm atmospheric window. *Remote Sens. of Environ.*, 47:345–361, 1994.

V. Salomonson. *Manual of Remote Sensing: Interpretation and Applications*, volume 2, chapter 29. American Society of Photogrammetry, The Sheridan Press, 1983.

M. B. Satterwhite and C. S. Allen. Reflectance spectra and optical depth of some sandy soils. In S. S. Shen and P. E. Lewis, editors, *Proceedings of SPIE – Volume 5806, Algorithms and Technologies for Multispectral, Hyperspectral, and Ultraspectral Imagery XI*, pages 542–553. SPIE, 2005.

M. B. Satterwhite, H. Mitchell, T. Hemmer, and J. D. Leckie. Field spectral signatures of snow, ice, and water. In S. S. Shen and P. E. Lewis, editors, *Proceedings of SPIE – Volume 5093, Algorithms and Technologies for Multispectral, Hyperspectral, and Ultraspectral Imagery IX*, pages 528–537. SPIE, 2003.

J. R. Schott. *Remote Sensing: The Image Chain Approach*. Oxford University Press, 1997.

E. Stoner and M. Baumgardner. Characteristic variations in reflectance of surface soils. *Soil Sci. Soc. Am. J.*, 45:1161–1165, 1981.

D. Thomas, R. E. J. Crosby, and J. Jafolla. Surface reflectance variations in realistic targets. In *Proceedings of SPIE – Volume 3375, Targets and Backgrounds: Characterization and Representation IV*, pages 27–38. SPIE, 1998.